The Institute of Space and Astronautical Science
Report No. 613, September 1984

An Experimental Study of Spray Thruster

By

Takao DOI, Seiichi YASUDA and Ryojiro AKIBA

(June 15, 1984)

Summary: The forced evaporation of liquid is employed to produce working fluid for a thermal thruster system called "Spray Thruster." The experimental model of spray thruster has been tested in the wide range of the mass flow rate using Ethyl Ether, Pentane and Furan. The spray thruster is operated well in a vacuum environment without any energy additions. The exhaust stream consists of vapor containing droplets, the mass fraction of which is in the range from 0.8 to 0.9. The Isp reaches 28 seconds at the propellant tank temperature of 20°C for Ethyl Ether. The analysis of the nozzle flow shows that an equilibrium flow model and partially frozen flow model explain properly the measured thrust performance in the small and large mass flow rate operations, respectively. The effects of chemical properties of propellant, nozzle scale, propellant tank temperature and structural mass of the system on the thrust performance have been investigated in detail to obtain the fundamental design aspects.

Key Words: Spray thruster, Evaporation process, Relaxation phenomena, Equilibrium flow model (EFM), Partially frozen flow model (PFFM)

NOTATION

A: nozzle cross sectional area
A_t: nozzle cross sectional area at throat
a: sonic speed
a_l: coefficient in Q_l
b_l: coefficient in Q_l
C_D: discharge coefficient
C_{Dp}: drag coefficient of particle (droplet)
C_F: thrust coefficient
C_p: heat capacity of liquid (droplet) phase
C_{pg}: heat capacity of gas (vapor) phase
C_v: discharge coefficient in a Venturi flow meter
C^*: characteristic velocity ($C^*=A_tP_0/\dot{m}$)
c_l: coefficient in Q_l
D_t: throat diameter
E_0: total enthalpy
F: thrust
g: gravitational acceleration
h_g: enthalpy of gas (vapor) phase

h_p: enthalpy of liquid (droplet) phase
I_e: effective specific impulse
I_{sp}: specific impulse
K: mass fraction of liquid phase
K_0: mass fraction of liquid phase in an evaporation chamber
L_c: axial length of evaporation chamber
L^*: characteristic length of evaporation chamber ($L^*=V_c/A_t$)
M_e: equilibrium Mach number
M_f: partially frozen Mach number
M_p: particle (droplet) material density
$\dot{m}$: mass flow rate
$\dot{m}_{ev}$: evaporating mass flow rate per unit area
N_u: Nuselt number
P: pressure
P_r: Prandtle number
P_s: saturstion vapor pressure
P_t: tank pressure
P_v: differential pressure
Q_l: latent heat of evaporation (function of temperature)
R: gas constant
R_e: Reynolds number defined by Eq. (A1–9)
R_{eth}: throat Reynolds number
r_p: radius of particle
S_w: allowable tensile stress
T: temperature
T_0: temperature in an evaporation chamber
T_c: temperature at critical point
T_f: temperature at freezing point
T_t: temperature in a propellant storage tank
U: velocity
U_0: characteristic velocity ($U_0=\sqrt{RT_0}$)
U_p: droplet frozen velocity
ΔV: characteristic velocity of auxiliary thruster system
V_c: volume of evaporation chamber
W_0: total mass of a rocket system
W_e: Weber number defined by Eq. (3–59)
W_p: propellant mass of auxiliary thruster system
W_p: payload mass
W_s: structural mass of auxiliary thruster system
W_t: structural mass of propellant storage tank
X_e: axial nozzle length of supersonic portion
X: axial coordinate
Y_c: inner radius of evaporation chamber
Y_{ic}: inner radius of nozzle wall at initial line for computation of PFFM

Y_t: throat radius
Y: radial coordinate
γ: specific heat ratio
ε: areal expansion ratio
η_{ST}: thrust efficiency of spray thruster
κ_g: coefficient of heat transfer by conduction in gas phase
κ_p: coefficient of heat transfer by conduction within a droplet
μ: viscosity of gas (vapor)
ν: frequency of chugging
ρ: density
ρ_w: density of tank wall material
σ: surface tension
τ_b: time constant of breakup
τ_c: time constant of heat transfer by conduction
τ_h: time constant of heat transfer by convection
τ_m: time constant of momentum transfer
τ_s: time constant of mass transfer
Φ: evaporating mass flow rate per unit volume

subscript

0: state in an evaporation chamber
e: equilibrium flow
ex: nozzle exit
f: partially frozen flow
L: liquid state
max: maximum value
p: particle (droplet) phase
s: saturation equilibrium
t: state in a storage tank

superscript

*: non-dimensional value

1. Introduction

Evaporation is driven mainly by the difference between the vapor pressure and the saturation pressure. Therefore exposing liquid into a vacuum environment results in strong evaporation, and the vapor-liquid or vapor-solid mixture is produced. The subliming solid rocket [*1,2*] and vaporizing liquid rocket [*3, 4*] utilize the evaporation process to produce gaseous working fluids. These thrusters are attractive as auxiliary propulsion systems due to the mechanical simplicity, low structural mass of the systems and storability of the propellants. They need, however, external heat sources to maintain the initial thrust magnitude. Their applicability is generally limited to the millinewton thrust range.

The working fluid is pure vapor in the subliming solid rocket and the vaporizing liquid rocket. The vapor stream in the nozzle has been investigated by many research-

ers [5, 6, 7]. It has been shown that nucleation and condensation occur in supersonic flow region and that small droplets appear in the flow field. Since the droplet diameter is generally smaller than 0.1 μm [5], the existence of these small particles seldom influence the thrust performance.

Relaxation phenomena between gaseous and condensed phases are momentum transfer, convective heat transfer, and mass transfer. Conductive heat transfer also exists within a droplet. Momentum and heat transfers have been the subject of many studies [8], especially in the case of the nozzle flow of metallized solid propellant rocket motors [9, 10, 11]. Since the particles which appear in such a flow field are oxidized metal particles, typically Al_2O_3 (Alumina), mass transfer between the phases is negligible. The combined mechanism of mass, momentum and energy transfer in multi-phase flow has been studied by few investigators.

Various relaxation phenomena including mass transfer have been treated in detail by Marble [12]. According to his analysis, the time constant of mass transfer is much smaller than those of the other relaxation processes. Since the mass transfer is driven by the difference between vapor pressure and saturation pressure, it means that saturation equilibrium is established in such a mixture flow field. Glenn [13, 14] numerically investigated the radial source flow of droplets expanding into vacuum. His computation showed that the evaporation process provided a sonic surface through which supersonic flow was attained. According to a practical point of view, the expansion phenomena of liquid into vacuum become important in such problems as propellant leakage from the tank and unusual behavior of liquid propellant rocket motor after misfiring in a space environment. However only qualitative works have been carried out experimentally by Mikatarion and Anderson [15]. Up to now, no positive application of liquid expansion into vacuum has been proposed.

In the present study, a proposal is made for a thruster system which produces thrust by accelerating a mixture of vapor and condensed phase through a nozzle. The principal advantages of this thruster are considered to be the wide range of the thrust level and the simplicity of the system. The thrust level is two or three orders of magnitude greater than those of the subliming solid rocket and the vaporizing liquid rocket. The present thruster system is very simple, because it does not need an external heat source nor a vapor-liquid separation mechanism. The simplification of the system brings higher reliability, mass and cost reductions. The present thruster can be called "Spray thruster," since it exhausts vapor-liquid or solid mixture like spray. The liquid propellant is injected directly into the thrust chamber, and then atomizes and evaporates. So the thrust chamber is named "Evaporation chamber." Since the latent heat of evaporation is transfered from the enthalpy of the injected liquid, the temperature of the liquid propellant stored in the tank remains constant. The working fluid is a mixture of vapor and droplets, the diameter of which is considered to be greater than 1 μm. Hence, the thrust production mechanism in the spray thruster is rather complicated due to various relaxation phenomena between vapor and liquid phases.

Let us consider the thermodynamic process of thrust production in order to under-

stand the characteristics of the spray thruster more clearly. A P-V diagram and T-S diagram for a typical thermodynamic substance are shown in Fig. 1-1 and Fig. 1-2. The solid line on the left side of the critical point is named the "saturation liquid line," and the solid line on the right side is named the "saturation vapor line." The broken line represents the constant liquid mass fraction. The expansion process of working fluid in the vaporizing liquid rocket is expressed by the path from state C to state D. Since the state of liquid stored in the tank corresponds to state A, an external heat source is necessary for the change from state A to state C. In the spray thruster, the expansion process is described from state A to state B. Both the path from state A to state C and the path from state A to state B are in the wet region. The shadowed domain indicates the magnitude of thrust. It is seen that the large difference between the spray thruster and the vaporizing liquid rocket operations is the magnitude of the liquid mass fraction. Effects of relaxation phenomena

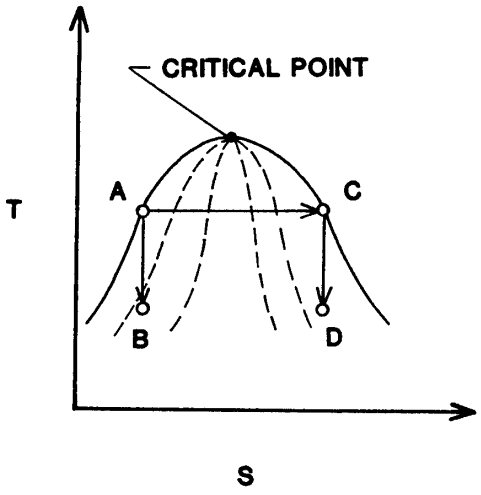

Fig. 1-1. T-S diagram.

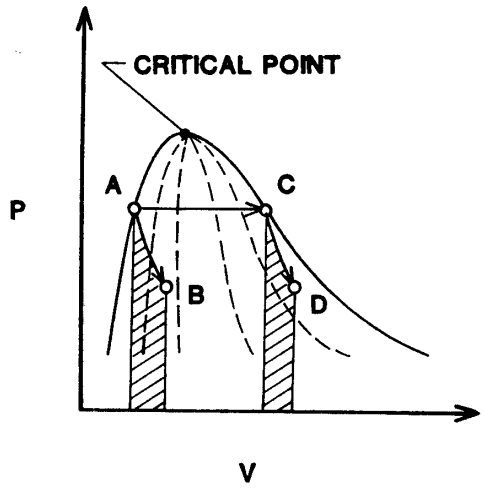

Fig. 1-2. P-V diagram.

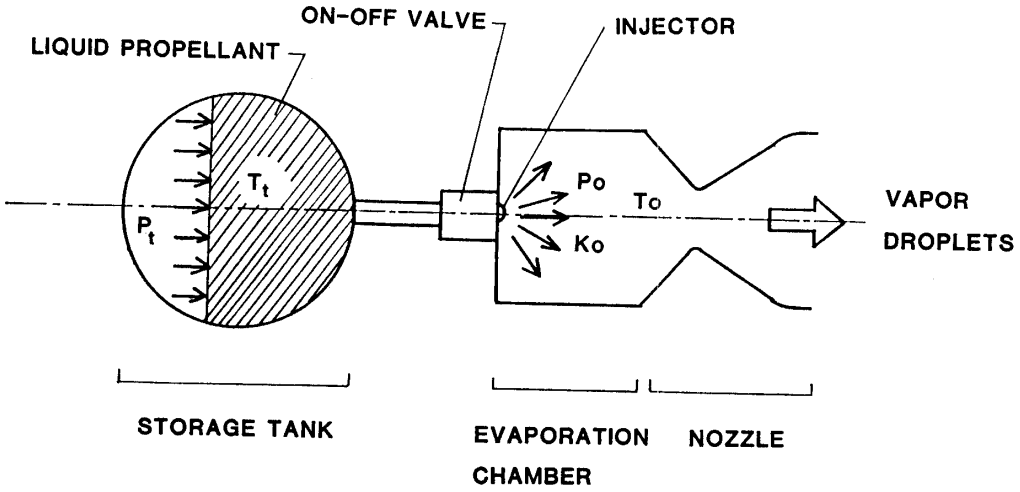

Fig. 1-3. Conceptual model of spray thruster.

on the thrust performance, then, become important in the spray thruster due to the large mass fraction of the liquid phase. It is also clearly shown that the liquid phase cannot evaporate completely through the isentropic expansion process.

Figure 1-3 shows a conceptual model of a spray thruster. The propellant fed from the pressurized tank is splashed through the injector into an evaporation chamber, in which some amount of liquid is evaporated. The temperature in the chamber is lower than in the tank, because the latent heat of evaporation is transfered from the enthalpy of the injected liquid phase. Since the time constant of evaporation process is generally very small, the chamber pressure is equal to the saturation vapor pressure. Therefore the thrust of spray thruster is approximately expressed by

$$F \approx P_s(T_0) \cdot A_t, \tag{1-1}$$

where F is the thrust, $P_s(T_0)$ is the saturation vapor pressure corresponding to the evaporation chamber temperature T_0, and A_t is the throat cross sectional area. The above equation is useful to evaluate liquid property, operational temperature and throat cross sectional area under a given thrust magnitude.

In order to clarify the characteristics of spray thruster performance, an experimental study has been carried out in Chapter 2. Based on the experimental results, the nozzle flows in the spray thruster have been theoretically investigated in Chapter 3. Two limiting models, "Equilibrium flow model" and "Partially frozen flow model" are examined in detail. In Chapter 4, the experimental results are compared with simulation results of the flow models, and the thrust performance characteristics are discussed. The effect of design parameter is also examined using the two theoretical flow models.

2. Experimental Study of Spray Thruster

Thrust performance of spray thruster is experimentally studied in this chapter. Spray thrusters have conventional configurations, which are composed of an electromagnetic valve, injector, evaporation chamber and convergent-divergent nozzle. Operational characteristics are investigated in the wide range of propellant mass flow rate. The thrust range of the present thruster is on the order of 1 N.

2–1. Properties of Liquid Propellant

Since a spray thruster utilizes the evaporation process of liquid to produce thrust, any liquids with vapor pressure are available as the propellant in principle. However it is necessary to consider the suitable properties of liquid in order to provide reasonable thrust level and specific impulse. The following features will be preferable.

Large heat capacity and small latent heat;

Latent heat of evaporation is transfered from enthalpy of the liquid phase, so that a large heat capacity and small latent heat are necessary in order not to decrease the working fluid temperature.

Low freezing point;

Thrust is very small when the working fluid temperature is close to the freezing point because the vapor pressure is very low in this range. In the preliminary experiment with use of 80°C water, an ice plug was formed at the exit of the nozzle and blocked the vapor flow. Therefore a low freezing point is also a necessary condition for high thrust performance and smooth operation.

Proper vapor pressure;

It is also necessary to select a liquid with a reasonable magnitude of vapor pressure, since the vapor pressure is one of the principal factors to determine the thrust level as indicated in Eq. (1-1).

Properties of various kinds of liquids are shown in Table 2-1. It is seen that latent heat of evaporation tends to increase with decreasing the molecular weight in general. Propane has been noticed to be an excellent propellant for the vaporizing liquid rocket due to the low latent heat of evaporation and low molecular weight [*3*]. It

Table 2-1. Properties of liquid [*30, 31, 32*].

Name	Molecular Weight	Critical Temp. (°C)	Freezing Temp. (°C)	Boiling Temp. (°C)	C_p at 25°C (J/(gK))	Q_l at 0°C (J/g)
Propane C_3H_8	44.1	96.8	−187.7	−42.1	0.15	33
Butane C_4H_{10}	58.12	152.0	−138.4	− 0.5	0.15	33
Pentane C_5H_{12}	72.15	196.6	−130.0	36.1	0.14	20 at 36
Ethyl ether $(C_2H_5)_2O$	74.12	194.6	−116.3	34.5	0.13	23
Ammonia NH_3	17.03	132.3	− 77.7	−33.3	0.26	72
Furan C_4H_4O	68.07	213.8	− 85.6	31.4	0.096	23 at 23
Water H_2O	18.0	374.1	0.0	100.0	0.24	143
Hydrazine N_2H_4	32.05	380.0	0.4	113.5	0.17	72 at 114
Methanol CH_4O	32.04	240.0	− 93.9	65.2	0.15	69 at 15
Freon 11 CCl_3F	137.37	198.0	−111.0	23.8	0.050	11
Mercury Hg	200.37	—	− 38.9	356.6	0.0079 at 25	16 at 358

Table 2-2. Evaporation properties of liquid [*30, 31, 32*].

	ETHYL ETHER	PENTANE	FURAN
a_l cal/g	104.41	118.31	107.27
b_l cal/(gK)	0.0784	0.1168	0.0784
c_l cal/(gK²)	−0.0004	−0.0008	−0.0004
A	6.985	6.852	6.975
B	1090.64	1064.63	1060.85
C	−42.0	−41.2	−45.5

$Q_l=a_l+b_lT+c_lT^2$, cal/g
$P_s=\exp[A-B/(C+T)]$, mmHg
T: Temperature, K

is, however, slightly difficult to handle Propane because it is in gaseous state at room temperature.

In the present experiment, Ethyl Ether, Pentane and Furan are chosen, since all of them are in liquid states at the standard condition and have relatively high vapor pressure. The evaporation properties of these liquids are given in Table 2-2. Chemical and physical properties of Ethyl Ether and Pentane are similar. As for Furan, the heat capacity is smaller than those of Ethyl Ether and Pentane.

2–2. Experimental Apparatus

2–2–1. A spray thruster

The experimental model of the spray thruster has a conventional configuration which is composed of an electromagnetic valve, injector, evaporation chamber and convergent-divergent nozzle. The schematic configuration of spray thruster is shown in Fig. 2-1.

The electromagnetic valve manufactured by Sterer Eng. & Mfg. Co. is operated in DC 24V. The response time for ON-OFF control is about 30 msec.

Two kinds of evaporation chambers were constructed. Both types are cylindrical. The inner diameter of the chamber is 20 mm for type-1, and 30 mm for type-2. The axial length of evaporation chamber can be varied by replacing spacers with various axial length. The spacers are made of either Stainless Steel or Teflon. The Teflon spacers have higher capability of thermal insulation, but any differences were not observed in measurement data obtained in the use of Stainless Steel and Teflon spacers.

The injector fills the role of both regulation of mass flow rate and atomization of propellant. The propellant was injected perpendicular to the thrust axis. This type of injection was adopted to avoid a contribution of feed pressure to the thrust, which could have been appreciable if the liquid had been injected in parallel to the thrust axis. In the present experiment, it is preferable to eliminate the contribution of the feed pressure in order to investigate the thrust production mechanism caused by the evaporation of liquid propellant. The detailed configuration of the injector is shown

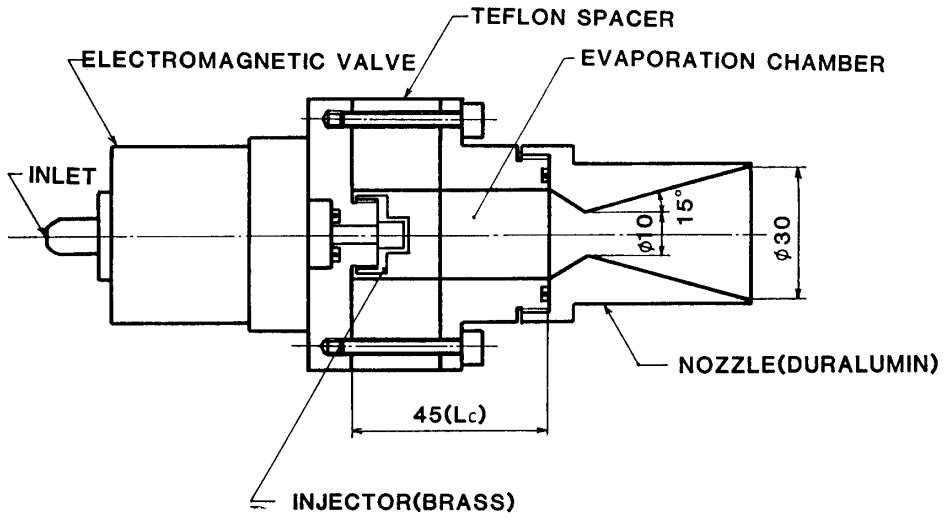

Fig. 2-1. Shematic configuration of spray thruster type-1.

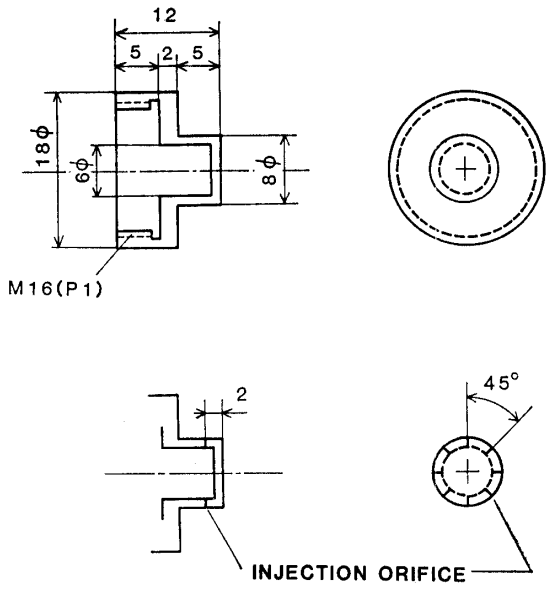

Fig. 2-2. Injector configuration.

in Fig. 2-2. The injector has orifices of 0.5 mm diameter on its cylindrical surface. The mass flow rate is varied in the wide range by replacing injectors with differing numbers of orifices. The injector is made of Brass.

The divergent portion of the nozzle is of a conical shape with a half apex cone angle of 15°. The throat diameter is specified to be 10 mm. The nozzle of type 1 is made of Duralumin, and type 2 is of 314 Stainless Steel.

2–2–2. Vacuum system

The present experiment was carried out using a vacuum chamber, the diameter of

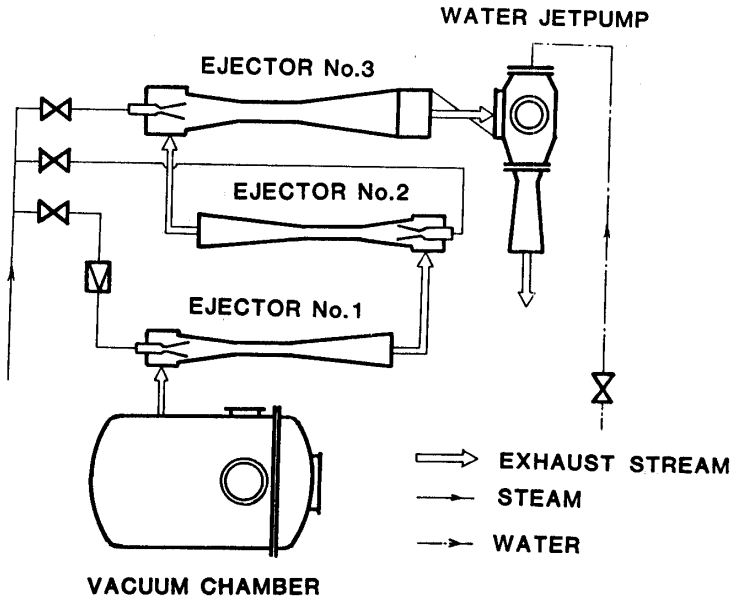

Fig. 2-3. Vacuum system.

which is 1.5 m, and volume is 3.55 m^3. The vacuum chamber is connected to a steam ejector system [*16*], and the background pressure is maintained less than 530 Pa throughout the thruster's operational duration. The ejector system is composed of three stage steam boosters and a water jet pump. The schematic of the vacuum system is shown in Fig. 2-3.

The vacuum facility used in the present experiment belongs to Japan's Institute of Space and Astronautical Science (ISAS).

2–2–3. Feed system

The liquid propellant was stored in a pressurized tank the diameter of which was 133 mm and height, 150 mm. The propellant tank and feed line were taped by electric heater. The propellant temperature was continuously monitored by using thermocouples and maintained at a fixed value by ON-OFF control in the heating circuit.

The liquid propellant was fed through a flowmeter to the thruster by N_2 (Nitrogen) gas pressure. Since a reservoir was provided between the propellant tank and a N_2 gas bomb, fluctuation in mass flow rate caused by N_2 gas pressure was suppressed to a negligible level.

2–2–4. Measurement system

Steady thrust, mass flow rate, pressure and temperature in the evaporation chamber were measured in the present experiment. The schematic measurement system is shown in Fig. 2-4.

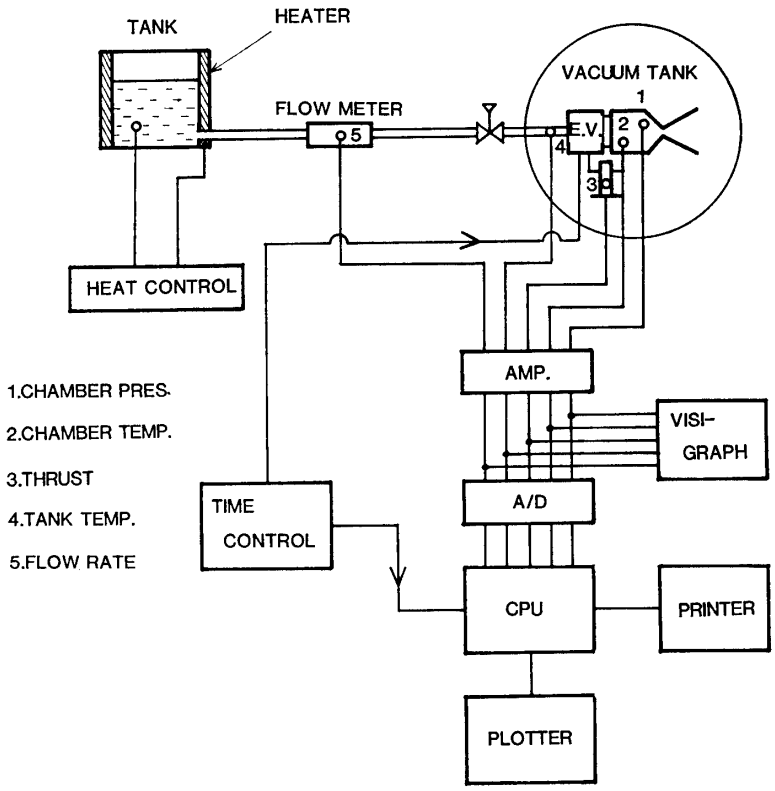

Fig. 2-4. Measurement system.

(A) Thrust measurement

Thrust was measured by a load cell of Shinkoh CK6-2K. The spray thruster is directly mounted on the load cell which stands perpendicularly on the measurement table as shown in Fig. 2-5. It is necessary to be careful so as to keep the center of gravity of the spray thruster on the center beam of the load cell in order to suppress the mechanical vibration.

Thrust magnitude was calibrated by suspending a known weight with a nylon string. A 573 gw dummy weight was continuously applied to the load cell to check the load cell-amplifier assembly. Thrust measurement error is estimated to be ±1% by the calibration.

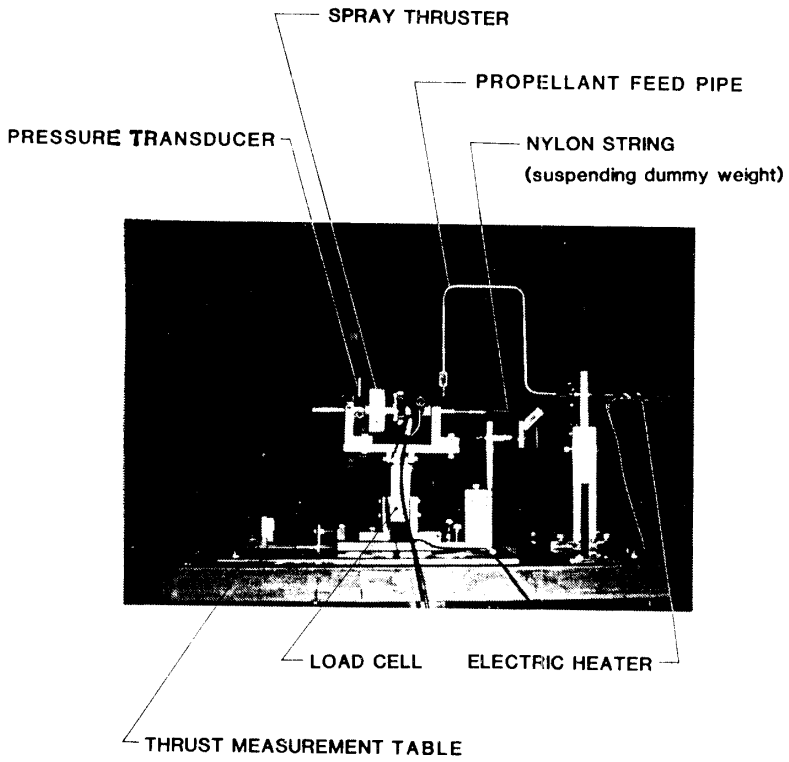

Fig. 2-5. Experimental apparatus in a vaccum chamber.

(B) Mass flow rate measurement

Two kinds of flow meters were used to measure the mass flow rate: A Venturi flow meter for mass flow rate greater than 30 cc/sec, and a turbine flow meter for the others.

The Venturi flow meter has an orifice of 6.1 mm diameter and cross sectional area ratio of 5.97. The mass flow rate is computed by the following equation:

$$\dot{m} = C_v \varepsilon A_0 \sqrt{2\rho P_v} / \sqrt{\varepsilon^2 - 1} \qquad (2\text{-}1)$$

where P_v is the differential pressure between the orifice and the duct. The ε is the cross sectional area ratio, A_0 is the cross sectional area of the orifice, C_v is the discharge coefficient, and ρ is the liquid density. Since the measurement accuracy of

the Venturi flow meter is poor in the low mass flow rate range, a Dodwell P-22 turbine flow meter is used for the mass flow rate range from 3 to 30 cc/sec.

Both flow meters were calibrated by flowing Ethyl Ether. The estimated errors of the measurement are 5% for the Venturi flow meter and 4% for the turbine flow meter.

(C) Pressure measurement

Evaporation chamber pressure was measured with Toyodakouki PD106 Piezoelectric Pressure Transducer, the measurement range of which was from 0 to 0.098 MPa absolute pressure.

It was calibrated by using Hg manometer to 1% accuracy.

(D) Temperature measurement

For temperature measurement, Copper-Constantan thermocouples of 0.25 mm diameter were used. The liquid propellant temperature was measured at the inlet of electromagnetic valve, and the temperature in the evaporation chamber by putting a thermocouple on the center axis of the spray thruster.

Calibration of thermocouple-amplifier assembly was carried out by immersion of the thermocouples in a fixed temperature water bath. The output values of the thermocouple were confirmed to be almost the same as the standard catalog values. The estimated measurement error is $\pm 0.5°C$.

(E) Data sampling system

All signals from the measurement instruments are converted to voltage signals, which are thereafter digitized by A/D converted and memorized on 8 bit microcomputer. Sampling number for one measurement channel is 2000, and eight channels are available in the present sampling system. Eight channel data are sampled in succession. Since the sampling speed is about 50 μ sec, the sampling time lag among eight channels is negligible. One data group is composed of successive eight channel data. The total measurement time can be varied by changing the sampling time between two neighboring data groups. In the present experiment, the sampling time of data group was chosen to be 2 msec. The total measurement time was 4 sec.

For the thrust measurement, the mechanical vibration component of the thrust stand was recorded on the data, and it was eliminated through a low pass filter of software.

The microcomputer used in the experiment is a Sharp MZ-80C.

2–3. Experimental Results

2–3–1. Steady state operation of spray thruster

The spray thruster was operated for 2 seconds. The tank temperature was fixed at 20°C. Typical measurement signals of thrust, evaporation chamber pressure and temperature are shown in Fig. 2-6 and Fig. 2-7. Figure 2-6 shows response characteristic of thruster type-1 with $L_c = 45$ mm. The spray thruster ran properly in a vacuum environment. The necessary build up time of the chamber pressure rising up to 90% of the steady state value is approximately 40 msec which is almost equal to the delay time for the electromagnetic valve to fully open. The thrust and chamber pressure do not immediately hit zero just after the electromagnetic valve is closed.

This is due to the fact that a small amount of liquid remains in a free volume between the valve and injector. The temperature record appears to decrease rapidly after the electromagnetic valve is shut off. This temperature fall is brought about by the evaporation of liquid wetting a surface of the thermocouple. The thrust curve is slightly regressive due to an increase in the background pressure during run.

For thruster type-2, low frequency instability was observed as shown in Fig. 2-7. This instability always occurred when the propellant feed pressure was below about 0.25 MPa absolute, but was not observed in the case of thruster type-1. The frequency of the oscillation is 20 Hz for $L_c=40$ mm and is 28 Hz for $L_c=20$ mm. The low frequency instability which is often observed in liquid propellant motor is called "chugging" [*17*]. The main cause is pressure sensitive time lag of gas production in the chamber. Typical frequency of the instability ν is given by

$$\nu=RT_0/(2\pi C^*L^*) \tag{2-2}$$

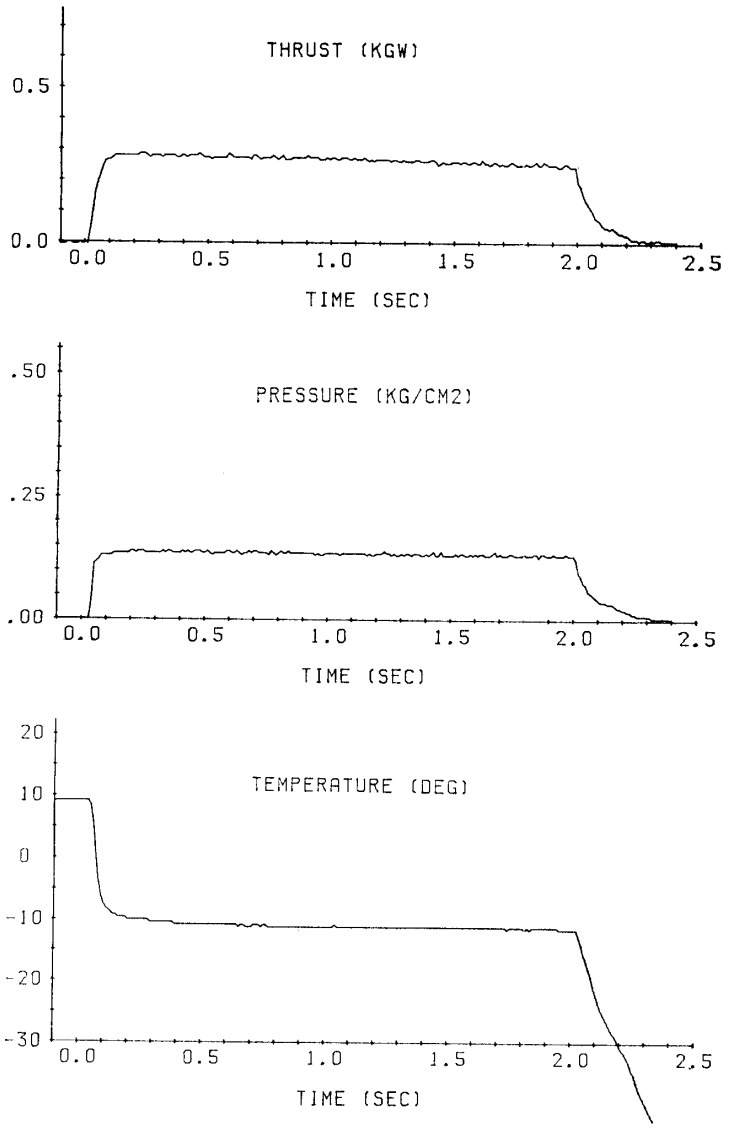

Fig. 2–6. Response characteristics of thruster type-1, feed pressure: 0.29 MPa.

where R is the gas constant, T_0 is the chamber temperature, C^* is the characteristic velocity, and L^* is the characteristic chamber length [*18*]. The observed frequency is almost equal to the value calculated from the above equation, so that the present low frequency instability is considered to have the same mechanism as the chugging. The dependency on the chamber configuration may be qualitatively explained as follows. The transition from liquid to vapor mainly occurs in the moment when the injected liquid collides with the inner cylindrical surface of the chamber wall and breaks up into small droplets. As a result, the time delay of gas production becomes shorter as the chamber diameter is decreased. This could contribute to the reason why the low frequency instability was not observed for thruster type-1. Since this instability is easily eliminated by raising the propellant feed pressure, it does not become a serious problem for the operation of the spray thruster.

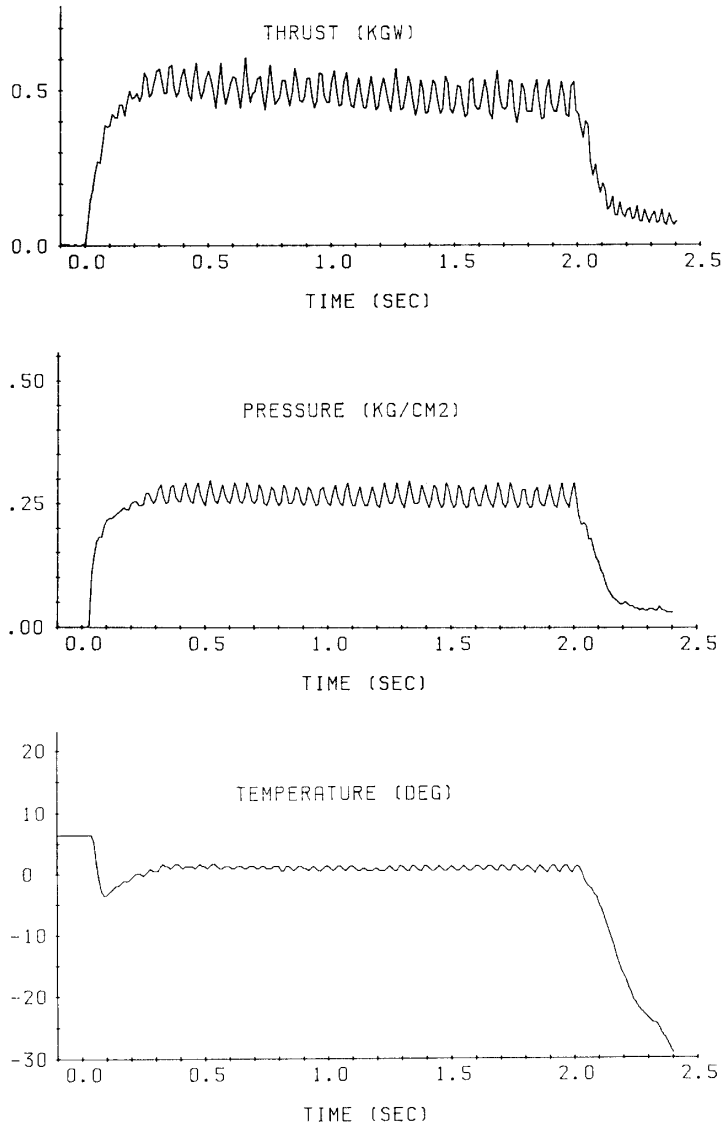

Fig. 2–7. Response characteristics of thruster type-2, feed pressure: 0.25 MPa.

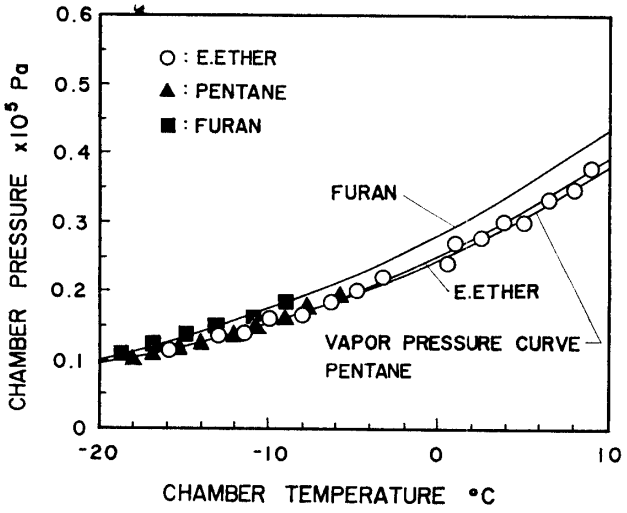

Fig. 2–8. Pressure-temperature characteristic in the evaporation chamber.

Figure 2-8 shows a relation between the pressure and the temperature in the evaporation chamber. Three solid lines represent the saturation pressure curves of liquid propellants. It is clearly seen that the saturation vapor pressure equilibrium holds at any operational temperature. It indicates that the time constant of the saturation equilibrium is enough smaller than the vapor stay time in the chamber.

As for the evaporation process in the chamber, the following assumptions can be made:

(1) Vapor and liquid phases have the same temperature.

(2) Injection process is adiabatic.

Assumption (1) is reasonable, since the droplet diameter is supposed to be smaller than the injector orifice diameter of 0.5 mm, and the time constants of heat transfer lie in the same order of the chamber stay time (See Section 3-1). Assumption (2) has been confirmed by the measurement of chamber wall temperature, which has been kept constant during the thruster operation. Under these assumptions, an energy conservation equation is derived as follows:

$$\dot{m}(1-K_0)\left\{\int_0^{T_0} C_p dT + Q_l(T_0)\right\} + \dot{m}K_0 \int_0^{T_0} C_p dT = \dot{m}\int_0^{T_t} C_p dT, \qquad (2\text{–}3)$$

where $\dot{m}$ is the mass flow rate, K_0 is the mass fraction of liquid phase, C_p is the heat capacity of liquid, T_0 is the evaporation chamber temperature, T_t is the tank temperature and $Q_l(T_0)$ is the latent heat of evaporation at temperature T_0. The first and the second terms in the left side of the equation represent enthalpy of vapor phase and liquid phase, respectively. The mass fraction of vapor phase is then given by

$$1-K_0 = \int_{T_0}^{T_t} C_p dT / Q_l(T_0). \qquad (2\text{–}4)$$

The mass fraction is plotted against the mass flow rate in Fig. 2-9. The vapor mass

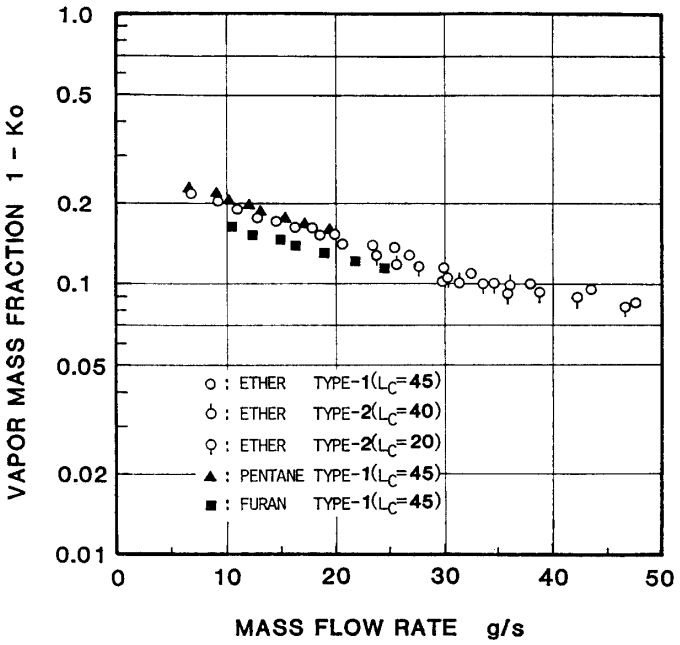

Fig. 2-9. Vapor mass fraction vs. mass flow rate.

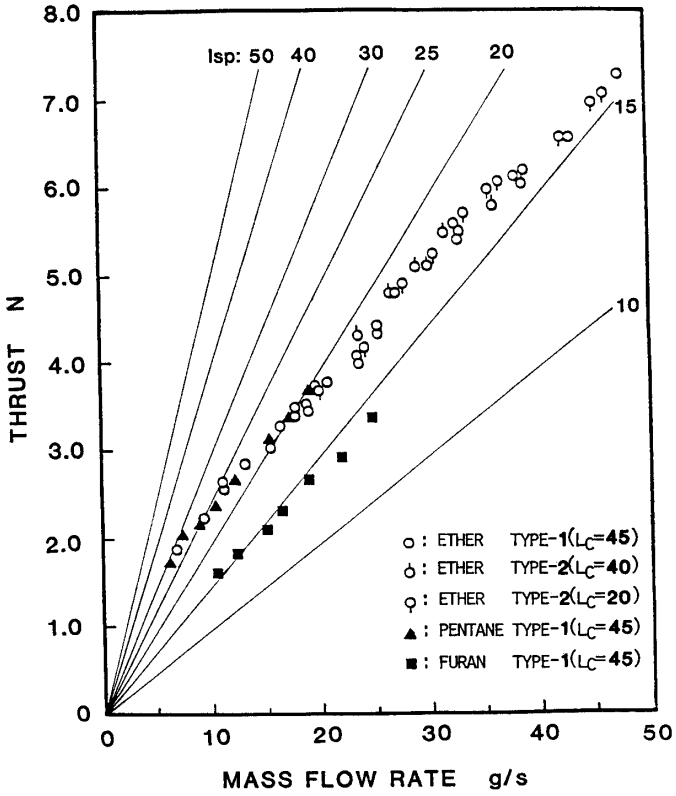

Fig. 2-10. Thrust vs. mass flow rate.

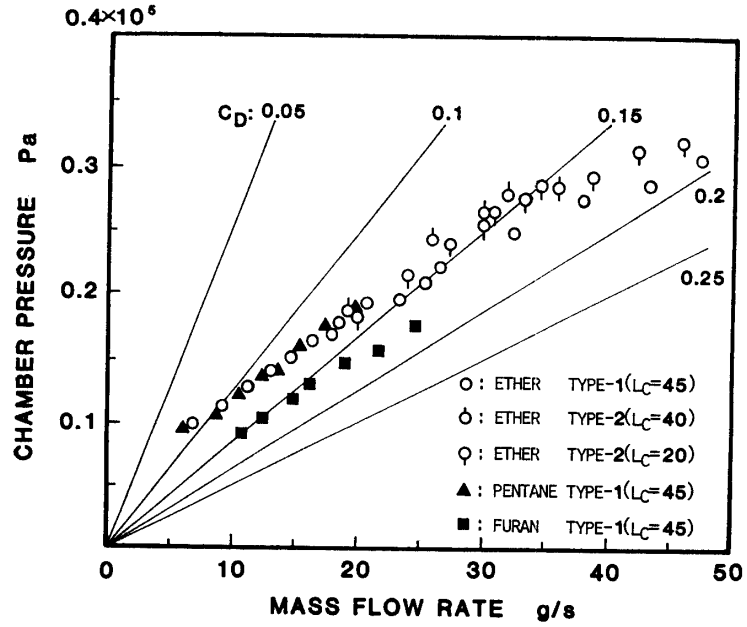

Fig. 2-11. Chamber pressure vs. mass flow rate.

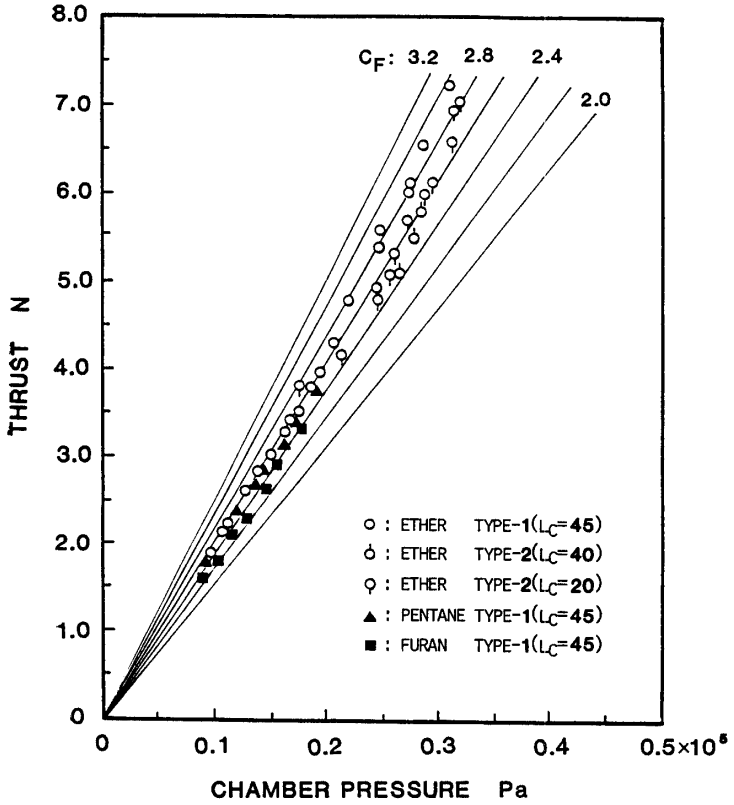

Fig. 2-12. Thrust vs. chamber pressure.

fraction of Ethyl Ether and Pentane is approximately 21% for $\dot{m}=7$g/s, and is decreased by increasing the mass flow rate. The vapor mass fraction of Furan is lower than those of Ethyl Ether and Pentane for a given mass flow rate.

Figures 2-10 to 2-12 show the relations among thrust, chamber pressure and mass flow rate. Thrust is plotted against mass flow rate in Fig. 2-10, in which solid lines represent specific impulse as is marked respectively. The specific impulse is defined by

$$I_{SP}=F/(g\dot{m}), \tag{2–5}$$

where F is the steady thrust, and g is the gravitational acceleration. With the use of Ethyl Ether, the specific impulse is 28 sec at mass flow rate of 6.9 g/sec and decreases asymptotically to 15 sec with increasing the mass flow rate. This is owing to an increase in the liquid mass fraction as shown in Fig. 2-9. Thrusters type-1 and type-2 give similar results. Pentane has almost the same thrust-mass flow rate characteristic as Ethyl Ether, but as to Furan the specific impulse is lower than those of Ethyl Ether and Pentane. This is attributed to the low specific heat of Furan, which allows considerable decrease in the working fluid temperature owing to the evaporation.

Chamber pressure is plotted against mass flow rate in Fig. 2-11, in which solid lines represent the discharge coefficient as is marked respectively. The discharge coefficient is defined by

$$C_D=\dot{m}g/(A_tP_0), \tag{2–6}$$

where A_t is the throat cross sectional area and P_0 is the chamber pressure. The C_D increases with the mass flow rate as the liquid mass fraction increases.

The relation between thrust and chamber pressure is shown in Fig. 2-12, in which solid lines denote the thrust coefficient as is marked respectively. The thrust coefficient is defined by

$$C_F=F/(A_tP_0). \tag{2–7}$$

The following relation results from Eqs. (2-5), (2-6) and (2-7):

$$C_F=C_D\cdot I_{SP}. \tag{2–8}$$

The C_F of various propellants are observed to be remarkably larger than that of ideal gas nozzle flow. This behavior is mainly caused by the large value of C_D associated with the large mass fraction of the liquid phase. In actuality, I_{SP} is varied with the mass flow rate, and an increase in I_{SP} compensates a decrease in C_D as the mass flow rate is decreased. It is a reason why C_F is observed to be almost constant in the wide range of the mass flow rate.

In the present experiment, it is shown that the spray thruster is operated properly in a vacuum environment, and that the saturation equilibrium state holds in the evaporation chamber. The large mass fraction of the liquid phase suggests that the behavior of liquid phase has great effects on the thrust performance. Figure 2-13

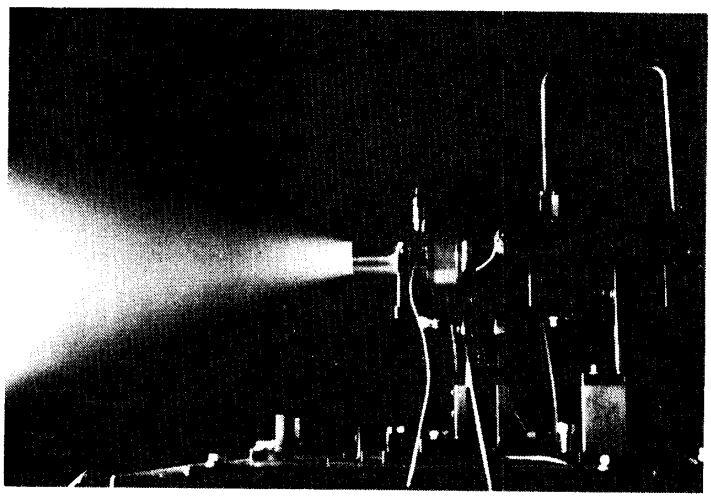

Fig. 2-13. Photograph of spray thruster in operation, mass flow rate: 25 g/sec.

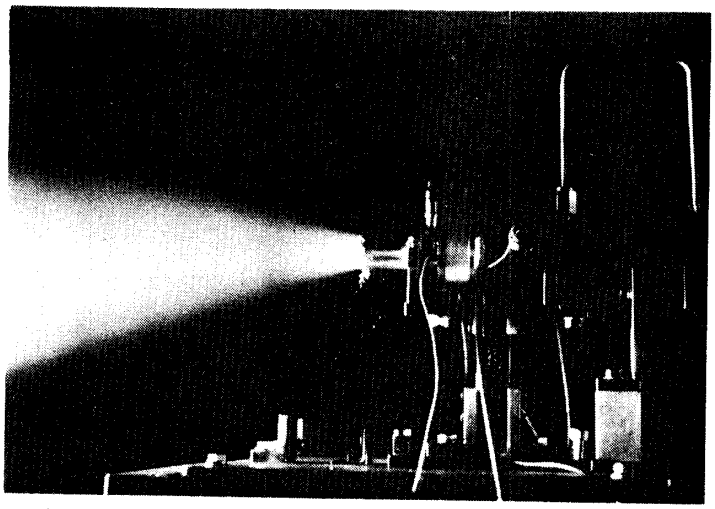

Fig. 2-14. Photograph of spray thruster in operation, mass flow rate: 42 g/sec.

shows the exhaust plume of the spray thruster. The plume is seen clearly since small droplets reflect the light, i.e., by the so-called Tyndall effect. In the operation of low mass flow rate, the plume is observed to expand uniformly. As the mass flow rate is increased, however, non-accelerated droplets are observed to disperse at the nozzle exit as shown in Fig. 2-14. These particles are considered to be evidence of formation of a thin liquid layer over the inner nozzle wall. The existence of the liquid layer gives one of the reasons why an increase in the mass flow rate reduces significantly the specific impulse.

2-3-2. *Thrust performance characteristics*

Thrust performance of the spray thruster has been described by using C_D, C_F, I_{SP} in the previous section. These characteristic parameters indicate only the integrated features of the spray thruster performance. In order to obtain more de-

tailed characteristics of the thrust performance, dependencies of C_D, C_F, I_{SP} on the evaporation chamber condition are discussed in the present section.

Reference mass flow rate described by state variables in the evaporation chamber can be defined as $\rho_{e0}U_0A_t$, where ρ_{e0} is the density of the mixture, U_0 is the characteristic velocity, and A_t is the throat cross sectional area. ρ_{e0} is equal to $P_0/\{(1-K_0\}RT_0\}$. When $\sqrt{RT_0}$ is adopted as the characteristic velocity, the reference mass flow rate is calculated using measurement values as follows:

$$\rho_{e0}U_0A_t=P_0A_t/\{(1-K_0)\sqrt{RT_0}\}. \tag{2-9}$$

Mass flow rate density, $\dot{m}/A_t$, which was measured in the experiment with thruster type-1, is plotted against $\rho_{e0}U_0$ in Fig. 2–15. All of data show good correlation. It should be noted that the difference of liquid species is not seen to have any effects in the figure. The following relation is obtained by a least squares regression analysis:

$$\dot{m}/A_t\propto(\rho_{e0}U_0)^{0.94}. \tag{2-10}$$

As for the discharge coefficient, the above equation reduces to

$$\begin{aligned}C_D&\propto[1/\{(1-K_0)\sqrt{RT_0}\}]^{0.94}(1/P_0)^{0.06}\\&=[Q_l(T_0)/\{C_p(T_t-T_0\}\sqrt{RT_0}\}]^{0.94}(1/P_0)^{0.06}.\end{aligned} \tag{2-11}$$

C_D depends on liquid properties, tank temperature, chamber temperature and pressure. It is noted that C_D is determined only by the temperature difference T_t-T_0 and the chamber temperature for a given liquid species, because $Q_l(T_0)$ and P_0 are functions of temperature.

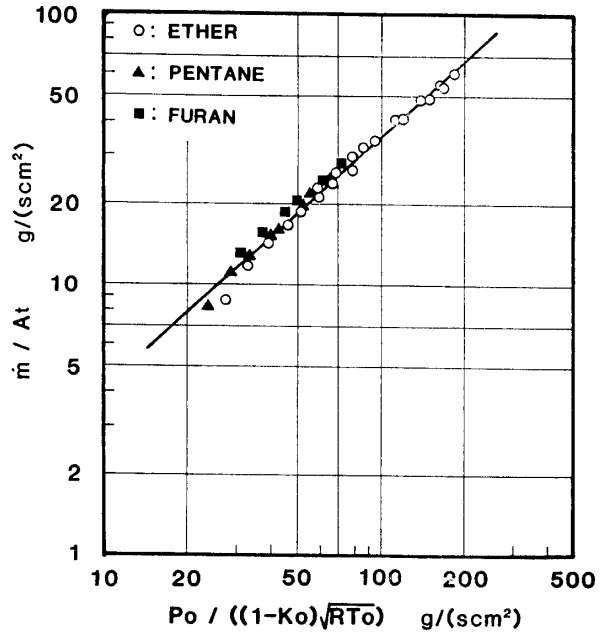

Fig. 2-15. Characteristics of mass flow rate density.

In a similar manner, reference thrust is defined as $\rho_{e0}U_0^2A_t$, which is also rewritten as follows:

$$\rho_{e0}U_0^2A_t=P_0A_t/(1-K_0). \tag{2-12}$$

The Measured thrust density, F/A_t, is plotted against $\rho_{e0}U_0^2$ in Fig. 2–16. It is shown that data points of Ethyl Ether and Furan are on different straight lines, the slopes of which are approximately same. The effect of liquid species indicated in Fig. 2-16 suggests that liquid properties affect the supersonic flow field in the divergent portion of nozzle, since C_D which is determined by the upstream condition of the throat does not show any dependency on liquid species. The following relation is obtained by a least square regression analysis:

$$F/A_t\propto\{P_0/(1-K_0)\}^{0.65}. \tag{2-13}$$

The above relation gives

$$C_F\propto\{1/(1-K_0)\}^{0.65}(1/P_0)^{0.35}. \tag{2-14}$$

The following correlation for I_{SP} is derived from Eqs. (2-8), (2-11), and (2-14):

$$I_{SP}\propto\{(1-K_0)/P_0\}^{0.29}(RT_0)^{0.47}. \tag{2-15}$$

The above relation is rewritten as

$$I_{SP}\propto[C_P(T_t-T_0)/\{Q_t(T_0)P_0\}]^{0.29}(RT_0)^{0.47}. \tag{2-16}$$

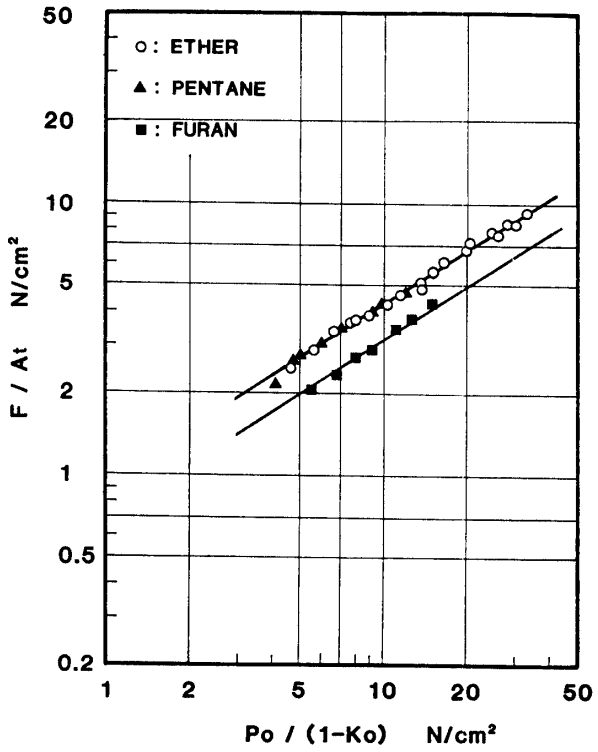

Fig. 2–16. Characteristics of thrust density.

Equations (2-11), (2-14), and (2-16) reveal the correlation of C_D, C_F, and I_{SP} with the evaporation chamber state variables. These correlations are insufficient for predicting the thrust value of the spray thruster on a quantitative base, but they can yield fundamental dependency of the thrust performance on liquid properties and operational temperature.

In Eq. (2-11), effect of P_0 on C_D is negligible. For a given liquid, Q_l and $\sqrt{RT_0}$ are regarded as fixed values within the present experimental range. Therefore C_D mainly depends on temperature difference T_t-T_0 and is decreased with increasing T_t-T_0. When the tank temperature is fixed, it is necessary to decrease T_0 in order to increase the vapor mass fraction in the chamber. As a result, terms of $(1-K_0)^{-0.65}$ and $P_0^{-0.35}$ in Eq. (2-14) change in opposite directions. This is an explanation that the measured value of C_F remains nearly constant. The dependency of I_{SP} on liquid properties and operational temperature is rather complex as indicated in Eq. (2-16). Effects of various parameters on I_{SP} are summarized as follows:

Heat capacity;
I_{SP} is proportional to $C_p^{0.29}$. The large C_p is preferable.

Latent heat of evaporation;
I_{SP} is inversely proportional to $Q_l^{0.29}$. The small Q_l is preferable.

Molecular weight;
I_{SP} is proportional to $R^{0.47}$. The large R, that is, small molecular weight is better. This relation is almost the same as that of ideal gas nozzle flow.

Operational temperature;
I_{SP} is proportional to temperature difference $(T_t-T_0)^{0.29}$ explicitly. However, I_{SP} is regarded as a complex function of T_0 since saturation vapor pressure and latent heat of evaporation are also functions of T_0. It is noted in the present experimental range that I_{SP} is increased with decreasing T_0. Large T_t is undoubtedly preferable.

3. Theoretical Study of Nozzle Flow

It has been clarified that the spray thruster is operated well using Ethyl Ether, Pentane and Furan as the propellant. The correlations of C_D, C_F and I_{SP} with state variables in the evaporation chamber have been obtained in the previous chapter. Since these correlations only describe integrated characteristics of the spray thruster, it is necessary to examine nozzle flow structure in order to understand the more detailed mechanism of thrust production. As one of the approaches, gas-particle nozzle flows with mass transfer are numerically investigated. Useful two theoretical flow models are presented in this chapter.

3-1. Models of Nozzle Flow

Nozzle flow is in general composed of a boundary layer along the nozzle wall and a core flow which is regarded as an inviscid region. It has been reported that the thrust loss in microthrusters increases and exceeds 10% when throat Reynolds number becomes less than 10^3 [*19*]. This is because of the development of the boundary layer in the nozzle flow field. On the contrary, as for thrusters the throat Reynolds number of which is larger than 10^4, the thrust loss attributed to the boundary layer is a few percent, and the thickness of the boundary layer is very thin. The throat Reynolds number is given by

$$R_{eth}=\rho U_{th}D_t/\mu, \tag{3-1}$$

where ρ is the flow density, U_{th} is the velocity at throat, D_t is throat diameter and μ is the viscosity. Since the thickness of the boundary layer is mainly subject to the behavior of the gas phase, the throat Reynolds number in the spray thruster is reasonably defined by using the state variables in the vapor phase. The mass flow rate of the vapor phase is approximately represented by $(1-K_0)\dot{m}$, so that Eq. (3-1) is rewritten as follows:

$$R_{eth}=4(1-K_0)\dot{m}/(\pi D_t\mu). \tag{3-2}$$

Since liquid mass fraction K_0 is approximately 0.9 in the present experimental range as shown in Fig. 2-9, the throat Reynolds number is increased with the mass flow rate. The throat Reynolds number at $\dot{m}=6.0$ g/sec is estimated to be 1.1×10^4. This result implies that the thrust performance characteristics of spray thruster are mainly subject to the structure of the core flow region.

On the other hand, the existence of a thin liquid layer along the nozzle wall was observed in the experiment. Effects of this layer on the thrust performance are supposed to be small in the low mass flow rate range because non-accelerated droplets were hardly observed in the lowest mass flow rate operation. In the large mass flow rate range, however, the effects of this liquid layer must be considered.

Fundamental equations of vapor-droplet flow in a quasi-one dimensional channel were derived by Marble [*12*] and Glenn [*13*] (See APPENDIX 2). These equations are fairly exact ones which take into account velocity and temperature relaxation processes between the vapor and liquid phases. But they contain so many parameters to be specified that they are not suitable for a comparative purpose with experimental results. In the present chapter, therefore, the author introduces simple and realistic flow models through the evaluation of time constants in various phenomena occurring in the flow field. As was mentioned in Chapter 1, the principal relaxation phenomena are mass transfer, momentum and heat transfer between the vapor and liquid phases, and conductive heat transfer within a droplet. The time constants of these phenomena are summarized in APPENDIX 1, and the results of adaptation to the present problem are listed in Table 3-1. The sample liquid is Ethyl Ether. It is assumed that the droplets are spherical and that the Reynolds number defined using velocity difference between vapor and droplet is so small that Stokes

Table 3-1. Time constants of relaxation phenomena, unit: sec.

Phenomenon	Formula	Droplet Diameter (μ)			
		1	10	100	1000
Mass Transfer	$\tau_s=\frac{M_p r_p}{3\rho\alpha a}$	10^{-6}	10^{-5}	10^{-4}	10^{-3}
Momentum Transfer	$\tau_m=\frac{2M_p r_p^2}{9\mu}$	10^{-5}	10^{-3}	10^{-1}	10
Heat Transfer (Liquid-Vapor)	$\tau_h=\frac{P_r M_p r_p^2}{3\mu}\cdot\frac{C_p}{C_{pg}}$	10^{-5}	10^{-3}	10^{-1}	10
Heat Transfer (in Droplet)	$\tau_c=\frac{M_p C_p r_p^2}{\pi^2\kappa_p}$	10^{-7}	10^{-5}	10^{-3}	10^{-1}
Chamber Stay Time	$\tau_0=\frac{\rho_0 V_c}{\dot{m}}$	10^{-2}	10^{-2}	10^{-2}	10^{-2}
Nozzle Flow	$\tau_t=\frac{D_t}{U_0}$	10^{-3}	10^{-3}	10^{-3}	10^{-3}

Table 3-2. Flow structures.

Particle Diameter (μ)	Relation of time constant	Flow structure
1	$\tau_c<\tau_s<\tau_f<\tau_m$	Equilibrium
10	$\tau_s=\tau_c<\tau_m<\tau_f$	Non-equilibrium
100	$\tau_s<\tau_c\leq\tau_f<\tau_m$	Non-equilibrium
1000	$\tau_s<\tau_f<\tau_c<\tau_m$	Partially Frozen

drag law is applicable.

The relaxation time of the mass transfer is proportional to the droplet diameter. It is smaller than those of momentum and heat transfer by convection. It is clearly shown that a saturation equilibrium condition holds throughout the nozzle flow field if the droplet diameter is smaller than 1 mm. The flow structure can be divided into four categories according to the droplet diameter as shown in Table 3-2. When the droplet diameter is less than 10 μm, all of relaxation processes are in equilibrium states. On the contrary, if the droplet diameter becomes larger than 100 μm, momentum and heat relaxation processes approach the frozen states. In the intermidiate case between both states, momentum and heat transfer are in non-equilibrium states. From the above evaluation, two limiting cases are observed to exist. The first is equilibrium flow which corresponds to the droplet diameter less than 10 μm. The other is a rather complicated state in which the mass transfer is in an equilibrium state, and momentum and heat transfer are in frozen states, which correspond to the droplet diameter larger than 100 μm. The latter case may be called "Partially frozen state". Both limiting cases are suitable for flow modeling, because uncertainties such as the droplet diameter distribution and the evaporation coefficient can be eliminated. In this respect, both equilibrium flow model and partially frozen flow model are discussed in detail in the following sections.

3–2. A Mathematical Model of Equilibrium Flow (EFM)

The following conditions are realized in equilibrium flow.

(1) Local pressure is equal to saturation pressure corresponding to the local temperature.
(2) Vapor velocity is equal to droplet velocity.
(3) Vapor temperature is equal to droplet temperature.
(4) Temperature is uniform within a droplet.

Under these conditions, the system of equations governing the flow field is derived as follows:

mass conservations:

$$\rho_e UA = \dot{m}, \tag{3–3}$$

momentum conservation:

$$\rho_e U dU/dX = -dP/dX, \tag{3–4}$$

energy conservation:

$$(1-K)\{h_p(T)+Q_l(T)\}+Kh_p(T)+U^2/2=E_0, \tag{3–5}$$

equation of state:

$$P=\rho RT, \tag{3–6}$$

where

$$\rho_e=\rho+\rho_p, \tag{3–7}$$

$$E_0=h_p(T_t)=\int_0^{T_t} C_p dT, \tag{3–8}$$

$$Q_l(T)=a_l+b_lT+c_lT^2. \tag{3–9}$$

The subscript p denotes the particle phase and ρ_e is the equilibrium flow density. It is convenient to describe the flow system with non-dimensional variables. Thus, let

$$\rho_e^*=\rho_e/\rho_{e0}, \quad U^*=U/U_0, \quad A^*=A/A_t, \quad X^*=X/Y_t,$$
$$P^*=P/P_0, \quad T^*=T/T_0,$$
$$h_p^*=h_p/(RT_0), \quad Q_l^*=Q_l/(RT_0), \quad C_p^*=C_p/R,$$
$$\dot{m}^*=\dot{m}/(\rho_{e0}U_0A_t), \quad F^*=F/(P_{e0}U_0^2A_t),$$

where the subscript 0 denotes the evaporation chamber properties, Y_t is the throat radius, and A_t is the throat cross sectional area. The system of non-dimensional equations is given as follows:

$$\rho_e^*U^*A^*=\dot{m}^*, \tag{3–10}$$

$$\rho_e^*U^*dU^*/dX^*=-(1-K_0)dP^*/dX^*, \tag{3–11}$$

$$(1-K)\{h_p^*(T^*)+Q_l^*(T^*)\}+Kh_p^*(T^*)+U^{*2}/2=E_0^*, \tag{3-12}$$

$$P^*=(1-K)\rho_e^*T^*/(1-K_0). \tag{3-13}$$

The saturation equilibrium condition is described by Clausius-Clapeyron equation:

$$dP^*/P^*=Q_l^*(T^*)dT^*/T^{*2}. \tag{3-14}$$

The acceleration condition of this flow system is given by

$$(1-M_e^2)dU^*/U^*+dA^*/A^*=0. \tag{3-15}$$

M_e is equilibrium flow Mach number defined as

$$M_e^2=\frac{U^{*2}}{(1-K)T^*}\left[1-\frac{2T^*}{Q_l^*}+\frac{1}{1-K}\cdot\frac{T^{*2}}{Q_l^{*2}}\left\{C_p^*+(1-K)\frac{dQ_l^*}{dT^*}\right\}\right]. \tag{3-16}$$

Local flow properties in this system are obtained as functions of non-dimensional temperature.

$$U^*=\left\{2T^*\int_1^{T^*}(1/T^{*2})\left(\int_{T_l^*}^{T^*}C_p^*dT^*\right)dT^*\right\}^{1/2}, \tag{3-17}$$

$$K=1-[E_0^*-\{h_p^*(T^*)+U^{*2}/2\}]/Q_l^*, \tag{3-18}$$

$$P^*=\exp\{a_l^*(1-1/T^*)+b_l^*\ln T^*-c_l^*(1-T^*)\}, \tag{3-19}$$

$$\rho_e^*=(1-K_0)P^*/\{(1-K)T\}, \tag{3-20}$$

$$A^*=\dot{m}^*/(\rho_e^*U^*). \tag{3-21}$$

Let C_p be constant, then, Eqs. (3-17) and (3-18) are rewritten in the following simple forms:

$$U^*=[2\{C_p^*T^*\ln T^*+E_0^*(1-T^*)\}]^{1/2}, \tag{3-22}$$

$$K=1-\{E_0^*T^*-(1+\ln T^*)C_p^*T^*\}/Q_l^*. \tag{3-23}$$

The mass flow rate is determined by choking condition at the throat:

$$M_e=1 \quad \text{at} \quad dA^*=0. \tag{3-24}$$

The flow temperature corresponding to $M_e=1$ is at first determined from Eqs. (3-16), (3-22), and (3-23). Then the flow velocity and density are obtained using Eqs. (3-22), (3-18), and (3-20). As a result, the critical mass flow rate is calculated from Eq. (3-21). The critical mass flow rate in the equilibrium flow is determined only by the evaporation chamber state and the throat diameter, and does not depend on the nozzle wall contour at the inlet portion.

In conventional chemical thruster systems, the temperature in the thrust chamber is almost independent of the mass flow rate and is usually determined by the chemical reactions of the propellant. Hence, the specific impulse is independent of the mass flow rate. On the contrary, the temperature in the evaporation chamber strongly depends on the mass flow rate in the spray thruster system. The temperature, pressure and liquid mass fraction in the evaporation chamber are adjusted to satisfy

the choking condition at the throat for a given mass flow rate. Therefore the specific impulse of the spray thruster considerably depends on the mass flow rate.

Non-dimentional thrust and I_{SP} in the equilibrium flow model are given with flow properties at the nozzle exit by

$$F^*=\{\rho_e^* U^{*2}+(1-K_0)P^*\}\cdot\varepsilon, \tag{3-25}$$

$$I_{SP}=U_0\cdot\{U^*+(1-K)T^*/U^*\}/g. \tag{3-26}$$

where ε is the areal expansion ratio.

In the following discussion, the equilibrim flow model is designated "EFM."

3-3. A Mathematical Model of Partially Frozen Flow (PFFM)

The partially frozen state is established when the droplet diameter becomes larger than 100 μm. An increase in the droplet diameter corresponds to the following situation: (See APPENDIX 1)

$$\tau_m \longrightarrow \infty \quad \text{and} \quad \tau_h \longrightarrow \infty, \tag{3-27}$$

where τ_m and τ_h are the time constants of momentum transfer and convective heat transfer between vapor and liquid phases, respectively. In the above limiting case, Eqs. (A2-4) and (A2-6) are rewritten as follows:

$$dU_p/dX=0, \tag{3-28}$$

$$\rho_p U_p dh_p/dX=-\Phi Q_l. \tag{3-29}$$

Eq. (3-28) denotes that the droplet velocity is frozen. But Eq. (3-29) indicates that the droplet temperature varies along the flow direction. In order to obtain a proper treatment for the droplet temperature, let us consider the evaporation mechanism of liquid. Evaporation is treated by a kinetic theory of molecules on the phase boundary. Molecules are emitted from the liquid surface with Maxwellian velocity distribution [*20*], and a Knudsen layer is formed over the liquid surface. Some amount of vapor molecules in a Knudsen layer is condensed into the phase boundary. The evaporation mass flow rate is then obtained as the difference between the emitted molecular mass and condensed molecular mass per unit time. The condensed molecules in general do not obey the Maxwellian velocity distribution [*21*]. Near to the saturation equilibrium condition, the evaporating mass flow rate is described by [*22*]

$$\dot{m}_{ev}=\frac{P}{\sqrt{2\pi RT}}\left\{C_1\frac{P_S(T_L)-P}{P}+C_2\frac{T-T_L}{T}\right\}, \tag{3-30}$$

where $P_S(T_L)$ is the saturation pressure corresponding to the liquid temperature T_L, C_1 and C_2 are the accomodation constants. In a free molecular flow in which condensed vapor molecules are assumed to have Maxwellian velocity distribution, C_1 and C_2 are calculated based on Hertz-Knudsen formula as

$$C_1=0 \quad \text{and} \quad C_2=0.5. \tag{3-31}$$

The saturation equilibrium condition which corresponds to $\dot{m}_{ev}=0$ in Eq. (3-30) gives

$$P=P_S \quad \text{and} \quad T=T_L. \tag{3-32}$$

It has been reported by Shankar [22] that the transition from free molecule to continuum is to suppress the dependence of the evaporation mass flow rate upon the temperature difference between the phases, i.e., to decrease the quantity of C_2. Since C_2 is small but non-zero, it must be reasonable to assume that Eq. (3-32) holds as the saturation equilibrium condition in the continuum state. It is expected that the droplet temperature becomes equal to the vapor temperature. Then the following conditions are assumed to be established for the partially frozen flow.

(1) Local pressure is equal to saturation pressure corresponding to the local temperature.
(2) Droplet velocity is frozen.
(3) Vapor temperature is equal to droplet temperature.
(4) Temperature is uniform within a droplet.

The system of equations governing this flow is given as follows:

mass conservation:

$$d(\rho UA)/dX=A\Phi, \tag{3-33}$$
$$d(\rho_p U_p A)/dX=-A\Phi, \tag{3-34}$$

momentum conservation:

$$\rho U dU/dX=-dP/dX+\Phi(U_p-U), \tag{3-35}$$
$$U_p=\text{const.}, \tag{3-36}$$

energy conservation:

$$(1-K)\{h_p(T)+Q_l(T)+U^2/2\}+K\{h_p(T)+U_p{}^2/2\}=E_0, \tag{3-37}$$

equation of state:

$$P=\rho RT, \tag{3-38}$$

where Φ denotes the evaporating mass flow rate per unit volume and unit time. The above system of equations is rewritten to the non-dimensional form in the same manner as in Section 3-2.

$$d(\rho^* U^* A^*)/dX^*=A^*\Phi^*, \tag{3-39}$$
$$d(\rho_p^* U_p^* A^*)/dX^*=-A\Phi^*, \tag{3-40}$$
$$\rho^* U^* dU^*/dX^*=-(1-K_0)dP^*/dX^*+\Phi^*(U_p^*-U^*), \tag{3-41}$$
$$U_p^*=\text{const.}, \tag{3-42}$$
$$(1-K)\{h_p^*(T^*)+Q_l^*(T^*)+U^{*2}/2\}+K\{h_p^*(T^*)+U_p^{*2}/2\}=E_0^*, \tag{3-43}$$
$$P^*=\rho^* T^*/(1-K_0), \tag{3-44}$$

where

$$\Phi^* = \Phi/(\rho_{e0} U_0 / Y_t). \tag{3-45}$$

The pressure is subject to Clausius-Clapeyron Equation (3-14). The acceleration condition in this system is obtained in the similar form to Eq. (3-15): (See APPENDIX 2)

$$(1-M_f^2)dU^*/U^* + dA^*/A^* = 0. \tag{3-46}$$

where M_f is partially frozen Mach number defined as follows:

$$M_f^2 = -\frac{1}{\theta_2}\left[U^{*2} + \left\{\theta_2\left(\frac{Q_t^*}{T^*} - 1\right) + \frac{C_p^* T^*}{1-K} + T^* \frac{dQ_t^*}{dT^*}\right\} \times \frac{1-(\theta_1/\theta_2)U^{*2}}{\theta_1/\theta_2\{C_p^* T^*/(1-K) + T^*(dQ_t^*/dT^*)\} \cdot (Q_t^*/U^{*2})}\right], \tag{3-47}$$

$$\theta_1 = (U^* - U_p^*)/U^*,$$

$$\theta_2 = U^{*2}/2 - U_p^{*2}/2 + Q_t^*.$$

The system has 9 dependent variables with 7 equations. When the nozzle shape is given, one additional condition is obtained by the choking condition at the throat. That is:

$$M_f = 1 \quad \text{at} \quad dA^* = 0. \tag{3-48}$$

This flow system can be solved numerically under these conditions. To determine another unknown parameter Up^*, the following assumption is further employed:

(5) The flow expands in equilibrium state from the evaporation chamber to the nozzle inlet.

This treatment is reasonable since the flow velocity in this region is small enough. The droplet frozen velocity is determined by this assumption to be equal to the equilibrium flow velocity at the nozzle inlet. Since the critical mass flow rate is obtained by solving the subsonic flow field, the nozzle inlet wall curvature affects the nozzle flow field in the partially frozen state. The well known Runge-Kutta method is employed as a computational integration technique.

In the large mass flow rate operation, a thin liquid layer was observed to be formed over the nozzle inner wall. The author thinks that under the assumption of negligible volume of the liquid phase, the present treatment of the partially frozen flow includes partly the effect of the thin liquid layer because this layer is considered to be formed by distributed droplets with frozen velocity over the nozzle inner wall. The more accurate influence of the liquid layer on the thrust performance will be obtained through the flow analysis taking into account of the core flow, the boundary layer, and the thin liquid layer.

Non-dimensional thrust and I_{SP} in the partially frozen flow are described with frow variables at the nozzle exit as follows:

$$F^* = (1-K)\dot{m}^* U^* + K\dot{m}^* U_p^* + (1-K_0)\varepsilon P^*, \tag{3-49}$$

$$I_{SP} = U_0 \cdot \{(1-K)U^* + U_p^* + (1-K_0\}\varepsilon P^*/\dot{m}\}/g. \tag{3-50}$$

In the following discussion, the partially frozen flow model is designated "PFFM."

3–4. Computational Results

Flow characteristics of EFM and PFFM are discussed in the present section for the nozzle configuration shown in Fig. 3–1, which is almost equal to that of thruster type-1. Numerical solutions presented here are confined to a single fluid, Ethyl Ether, and the evaporation chamber temperature is assumed to be constant. The fluid properties and the evaporation chamber condition are shown in Tabel 3-3.

Figures 3-2 to 3-4 illustrate the flow structures in EFM when the tank temperature is specified to be 273 K, 293 K and 313 K, respectively. The horizontal axis denotes dimensional nozzle exit radius, and the vertical axis denotes non-dimensional quantities of pressure, temperature, velocity, and liquid mass fraction. The flow temperature distribution is almost unchanged with an increase in the tank temperature, and is decreased monotonously throughout the nozzle flow field. The pressure is decreased rapidly in the vicinity of the throat, and approaches zero with increasing the nozzle exit area. The liquid mass fraction is also reduced with increasing the nozzle exit area, which indicates that the evaporation takes place throughout the nozzle flow field. The strong evaporation is observed near the throat section. The liquid mass fraction in the evaporation chamber is reduced approximately to 0.1 as the tank temperature increases by 20°C. The flow velocity is increased monotonously

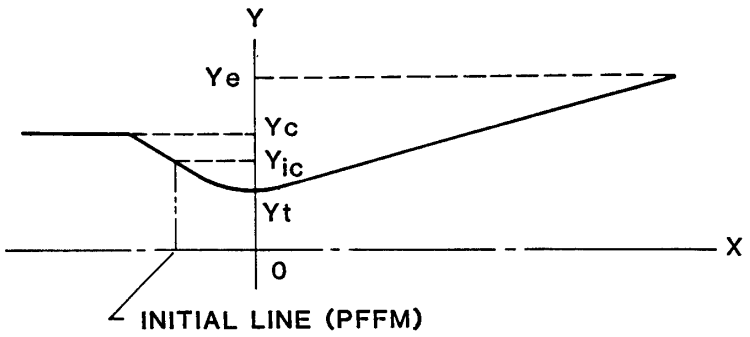

Nozzle cofiguration for numerical calculation.

$X^*=-2.268$: $Y^*=2.0$

$-2.268<X^*<-1.0$: $Y^*=-0.577X^*+0.691$

$-1.0<X^*<0.258$: $Y^*=-\sqrt{2^2-X^{*2}}$

$0.258<X^*<7.727$: $Y^*=0.268X^*+0.929$

Fig. 3-1. Nozzle configuration.

Table 3-3. Evaporation chamber conditions.

T_0:	260K
P_0:	12910 Pa
ρ_0:	0.443 kg/m^3
U_0:	171 m/s

with the nozzle exit area and shows strong dependence on the tank temperature. For instance, an increase in the tank temperature from 273 K to 313 K results in 100 m/sec increase in the velocity at $Ye^*=10$.

Since the convergent portion of the nozzle affects the choked condition in PFFM as was discussed in Section 3-3, the effect of the position of initial line for computation on the flow structure in PFFM is at first examined. Figure 3-5 shows behaviors

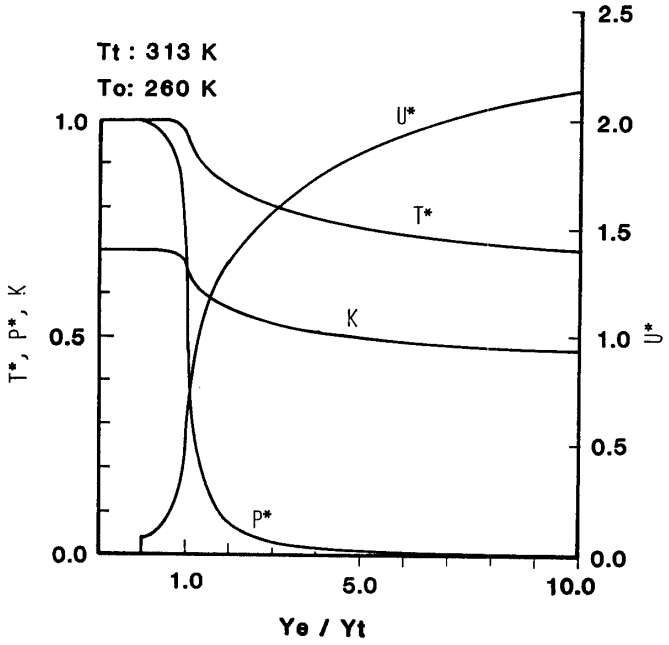

Fig. 3-2. Flow structure in EFM, T_t=313K, T_0=260K.

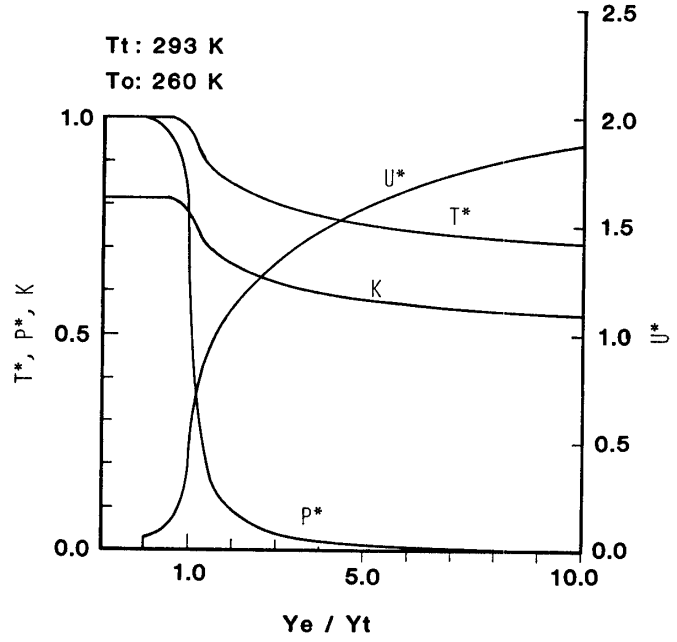

Fig. 3-3. Flow structure in EFM, T_t=293K, T_0=260K.

of flow properties at expansion ratio of 9, in which the initial line is moved from the geometrical nozzle inlet to the throat. Y_c and Y_{ic} denote the radius of nozzle wall at the nozzle inlet and the initial line, respectively. The variations of thrust, mass flow rate, and liquid mass fraction are negligible when $(Y_c-Y_{ic})/Y_t$ is less than 0.5. The vapor and droplet velocities are almost constants when $(Y_c-Y_{ic})/Y_t$ is less than 0.2. With increasing $(Y_c-Y_{ic})/Y_t$, $\dot{m}^*$ and F^* are decreased. This is attributed to the fact that the frozen flow structure becomes similar to that in EFM as the initial condition line approaches the throat. From these observation, it is concluded that the typi-

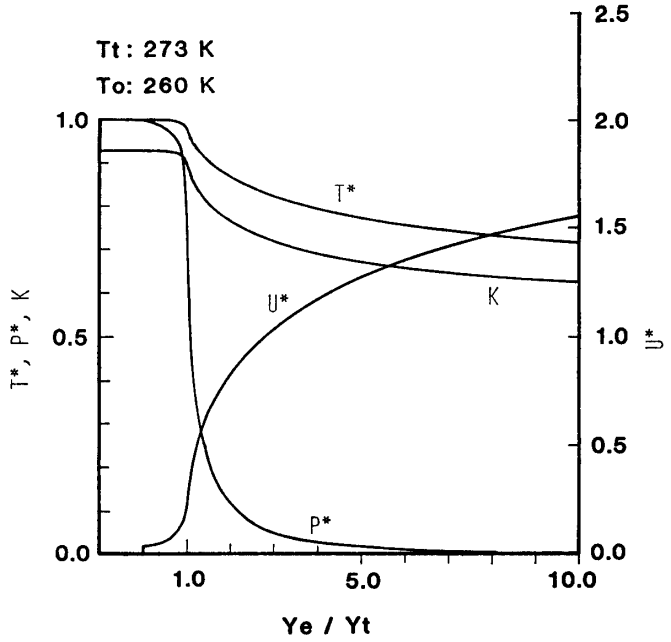

Fig. 3-4. Flow structure in EFM, T_t=273K, T_0=260K.

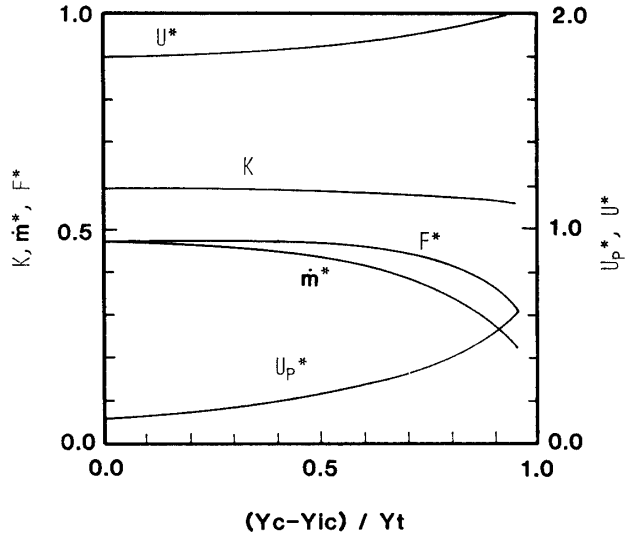

Fig. 3-5. Effect of the position of initial line on the flow structure at expansion ratio of 9.

cal flow structure in PFFM is reasonably described by setting the initial line on the geometrical nozzle inlet, that is, by putting $Y_{ic}=Y_e$. The following calculation for PFFM is carried out under this condition.

Figures 3-6 to 3-8 illustrate the flow structures in PFFM, in which the tank temperature is varied from 273 K to 293 K, 313 K, respectively. The temperature,

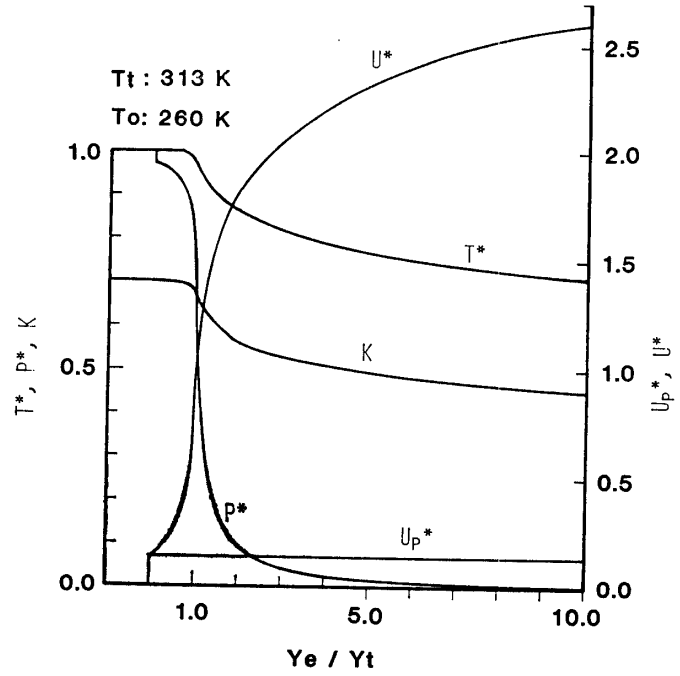

Fig. 3-6. Flow structure in PFFM, T_t=313K, T_0=260K.

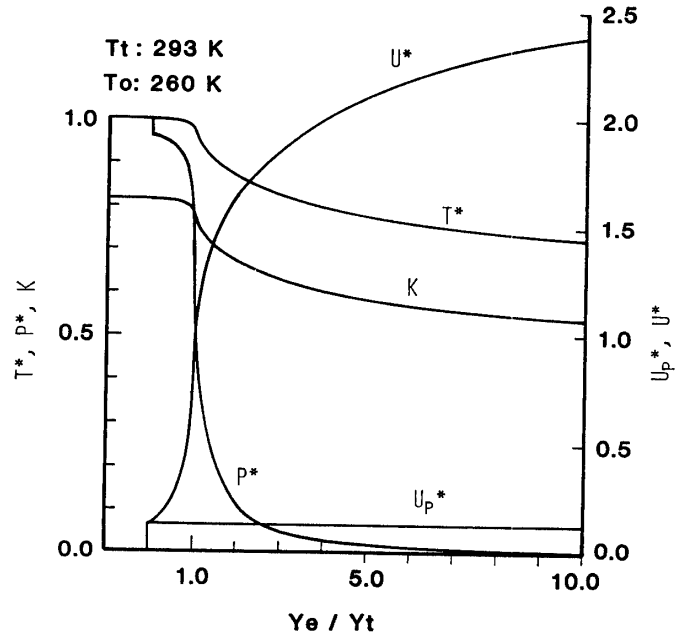

Fig. 3-7. Flow structure in PFFM, T_t=293K, T_0=260K.

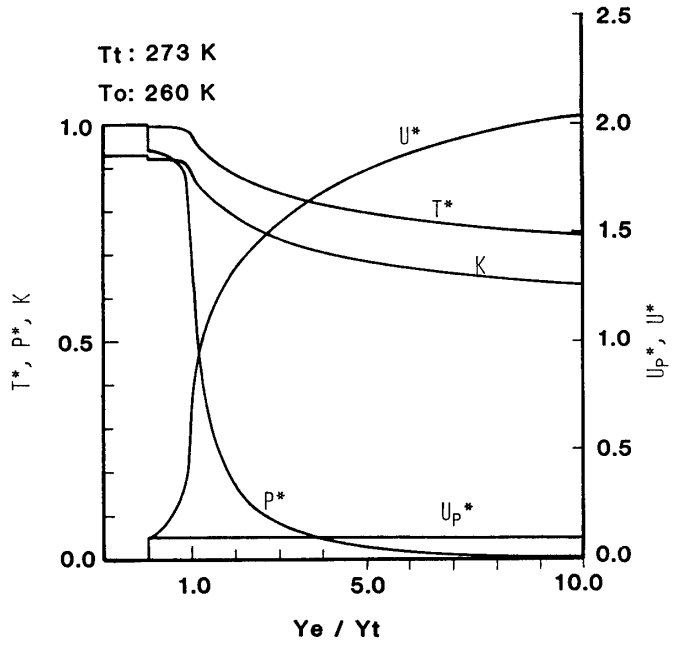

Fig. 3-8. Flow structure in PFFM, T_t=273K, T_0=260K.

pressure, vapor velocity, and liquid mass fraction distributions are shown to have the same tendencies as those of EFM. For a given tank temperature, the flow temperature and the liquid mass fraction are almost equal to those of EFM throughout the nozzle flow field. The vapor velocity in PFFM is larger than the equilibrium flow velocity in EFM, because only the vapor phase is accelerated in PFFM. The vapor velocity reaches to approximately 445 m/sec at Ye^*=10 at the tank temperature of 313 K. This velocity is about 80 m/sec faster than the equilibrium flow velocity. The droplet velocity is fixed to be about 20 m/sec, even if the tank temperature is altered in the wide range. Figure 3-9 shows the variations of thrust coefficient in both EFM and PFFM which are denoted by the solid and the broken lines, respectively. The thrust coefficient of both models is increased monotonously with the nozzle exit radius. The thrust in PFFM is larger than that in EFM for a given tank temperature. The lower the tank temperature is, the larger is the thrust coefficient in both models. These tendencies are explained as follows. Discharge coefficient C_D for various flow conditions is given as

T_t:	273K	293K	313K
C_D (*EFM*):	0. 0976	0. 0762	0. 0603
C_D (*PFFM*):	0. 270	0. 145	0. 101

C_D is increased with decreasing the tank temperature. C_D in PFFM is much larger than that in EFM. The large quantity of C_D, that is, large mass flow rate results in both large thrust and large thrust coefficient for a given nozzle wall configuration.

Readers may ask whether the evaporation process in the supersonic flow field contributes always to the thrust production or not. The answer to this question is given through the following consideration. The kinetic energy of the flow is ex-

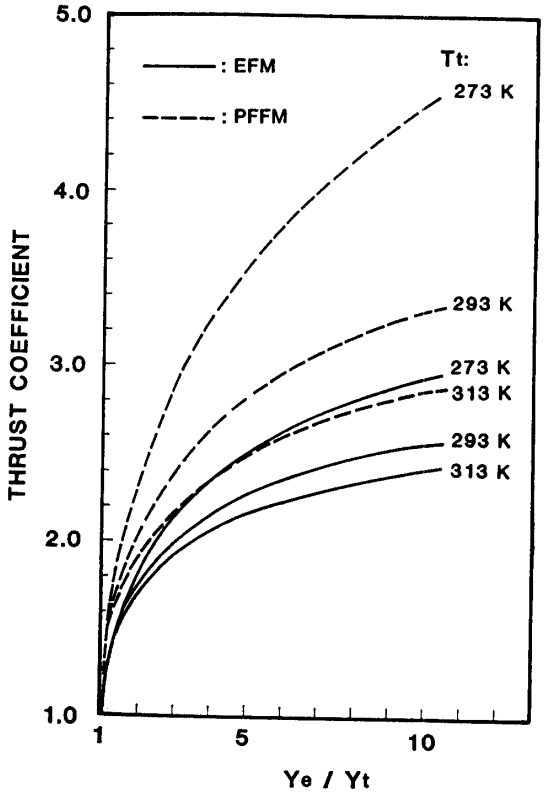

Fig. 3-9. Variation of thrust coefficient.

pressed as $\dot{m}U^2/2$. Since $\dot{m}$ is put to be constant, the kinetic energy is proportional to U^2. The non-dimensional expression for $U^2/2$ is given employing Eq. (3-22) by

$$U^{*2}/2=C_p^*T^*\ln T^*+E_0^*(1-T^*). \tag{3-51}$$

Differentiating the above equation with respect to X^*,

$$d(U^{*2}/2)/dX^*=(1-T_t^*+\ln T^*)C_p^*\cdot dT^*/dX^*. \tag{3-52}$$

Since T_t^* is larger than unity and $\ln T^*$ is negative, a positive value of $d(U^{*2}/2)/dX^*$ corresponds to a negative value of dT^*/dX^*. On the other hand, differentiation of Eq. (3-18) with respect to X^* results in

$$dK/dX^*=-\{(a_i^*-c_i^*T^{*2})(1-K)/T^*-C_p^*\}/Q_i^*\cdot dT^*/dX^*, \tag{3-53}$$

where $Q_i^*=a_i^*+b_i^*T^*+c_i^*T^{*2}$. Elimination of dT^*/dX^* from Eq. (3-52) and Eq. (3-53) leads to

$$d(U^{*2}/2)/dX=-\frac{(1-T_t^*+\ln T^*)T^*Q_i^*C_p^*}{(a_i^*-c_i^*T^{*2})(1-K)-C_p^*}\cdot dK/dX^*. \tag{3-54}$$

From the above equation, the necessary conditions for $d(U^{*2}/2)/dX^*>0$ are obtained as follows:

$$(a_l^* - c_l^* T^{*2})(1-K) < C_p^* \quad \text{and} \quad dK/dX^* < 0, \tag{3-55}$$

$$(a_l^* - c_l^* T^{*2})(1-K) > C_p^* \quad \text{and} \quad dK/dX^* > 0. \tag{3-56}$$

Then, it is concluded that the evaporation process contributes to the thrust production only when the flow properties satisfy the condition: $(a_l^* - c_l^* T^{*2})(1-K) < C_p^*$. When $(a_l^* - c_l^* T^{*2})(1-K) > C_p^*$, the condensation process occurs. In the present experimental range, the quantity of $(a_l^* - c_l^* T^{*2})(1-K) - C_p^*$ is always positive for Ethyl Ether. The evaporation process contributes to the thrust production.

It is known that when a droplet is subjected to a gas flow with a relative velocity in excess of some critical value it disintegrates or shatters. Such a phenomenon is called "breakup" and it was investigated by many researchers [*23 24, 25*] The breakup of droplet is an important process in the spray thruster, because the droplet diameter affects significantly the thrust performance. A droplet placed in a vapor stream will break when the force due to the variation of aerodynamic pressure over the droplet exceeds the surface force, which is depending on the surface tension and the curvature of the droplet. For a spherical droplet, the surface force is expressed by $2\sigma/r_p$. The condition of breakup is, then, approximately given by

$$\frac{1}{2} C_{Dp} \rho (U - U_p)^2 \geq 2\sigma / r_p. \tag{3-57}$$

where C_{Dp} is the drag coefficient of spherical droplet [*26*]. The above equation is rewritten by using Weber number W_e as follows:

$$C_{Dp} \cdot W_e \geq 8. \tag{3-58}$$

The weber number is defined by

$$W_e = \rho (U - U_p)^2 2 r_p / \sigma, \tag{3-59}$$

which means the ratio of aerodynamic drag force and surface tension [*24*]. In the case of small droplet, where the Stokes drag law is applicable, the following expression of Eq. (3-58) is obtained by using Eq. (A1-8):

$$W_e / R_e \geq 1/3, \tag{3-60}$$

where R_e is the Reynolds number defined by Eq. (A1-9). In the case of large droplet, the Reynolds number of which exceeds unity, C_{Dp} is equal to about 0.4 [*27*]. Thus, Eq. (3-58) is rewritten as follows:

$$W_e \geq 20. \tag{3-61}$$

The existence of critical value of Weber number is confirmed by several experiments [*23, 24*]. The critical value of 20 in Eq. (3-61) is about twice the value found from the experiment [*23*]. An overestimate is considered to be due to the deformation of droplet observed before it bursts.

For the spray thruster, the Reynolds number and Weber number are calculated by using PFFM to evaluate the possibility of occurrence of breakup in the nozzle. The

computational condition is that the tank temperature is 293 K, the evaporation chamber temperature is 260 K, and the propellant is Ethyl Ehter. The viscosity and surface tension are assumed to be 6.8×10^{-6} kg/(msec) and 1.7×10^{-2} N/m, respectively. The results are shown in Fig. 3-10. The Reynolds number is larger than unity over the nozzle flow field, so that the breakup condition is given by Eq. (3-61). For a droplet of 100 μm in diameter, the W_e is smaller than 10. Thus, the droplet will not break up in the nozzle. On the other hand, for a droplet of 1000 μm in diameter, the W_e exceeds 20 near the throat. The breakup of droplet may occur in this case. The maximum Weber number is obtained at $Y/Y_t=1.2$ in supersonic flow region. The maximum allowable diameter is calculated to be 308 μm, when the critical Weber number is set to be equal to 20.

One additional factor which should be considered is the time constant of breakup. Gordon [*28*] and Morrell [*29*] gave the folowing expression of the time constant:

$$\tau_b=\frac{4r_p}{|U-U_p|}\cdot\sqrt{\frac{M_p}{\rho}}. \tag{3-62}$$

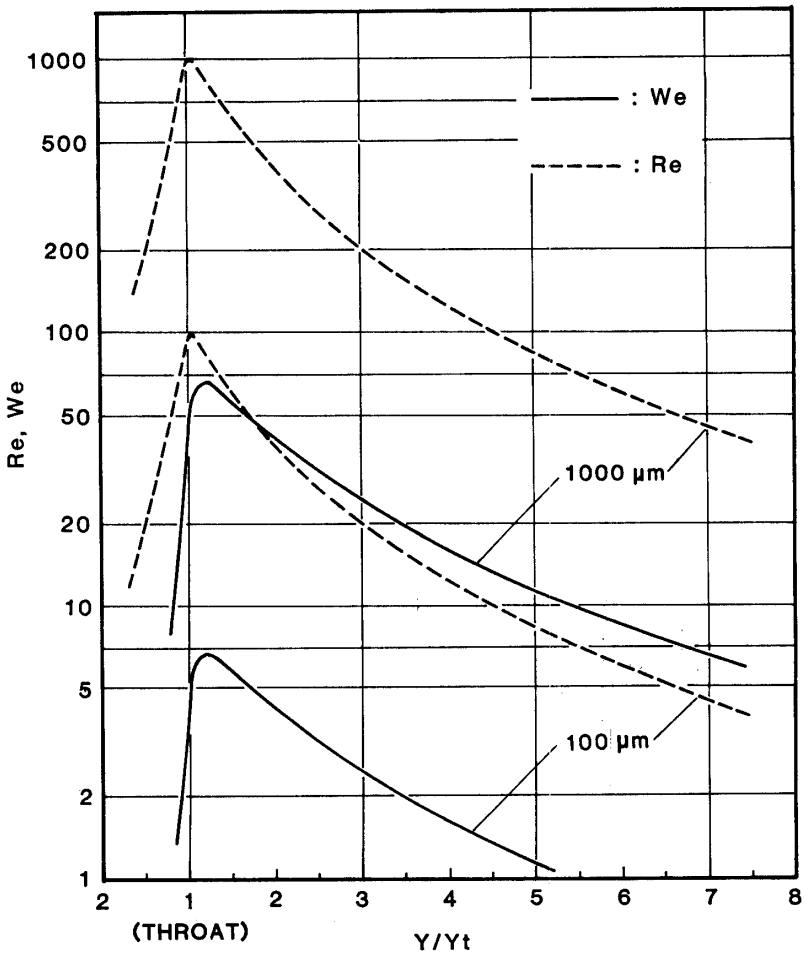

Fig. 3-10. Variation of Weber number and Reynolds number in the nozzle. Flow model: PFFM.

For the case of droplet of 308 μm in diameter, the τ_b is estimated to be 0.6 msec. Since the τ_b is smaller than the droplet stay time in the nozzle, the breakup process finishes completely within the nozzle.

Above consideration of breakup of droplet shows that an upper limit value exists in the droplet diameter in the spray thruster. The predicted maximum value lies in the diameter range of partially frozen flow model (PFFM). If the breakup of droplets occurs, the nozzle flowfield will become more complicated. The present evaluation suggests that a flow model which combines PFFM for the subsonic flow region with EFM for the supersonic one may be suitable for describing such a flow field with breakup of droplets.

4. Discussion

4–1. Comparison of Experimental Results with Numerical Simulation

Thrust performance characteristics of the spray thruster are discussed in the present section comparing experimental results with numerical simulation. The numerical calculation has been carried out putting the tank temperature and the evaporation chamber temperature equal to the experimental condition. The nozzle configuration of thruster type-1 is adopted for the computation. The calculated quasi-one dimensional thrust is modified by multiplying the correction factor $(1+\cos\theta)/2$, where θ is a half apex cone angle of the conical nozzle.

Figure 4–1 shows the relation between mass flow rate density and reference mass flow rate density described with the evaporation chamber state variables. The calculated results for Ethyl Ether and Furan in PFFM are almost identical, which are

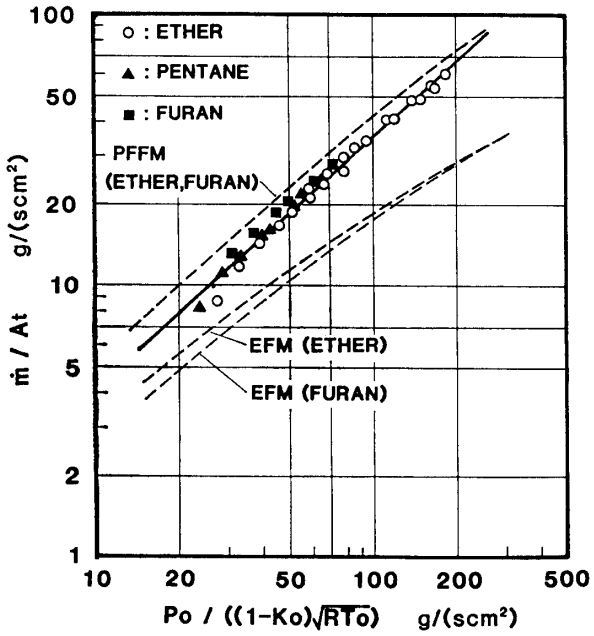

Fig. 4–1. Comparison of experimental results with numerical ones: characteristics of mass flow rate density.

illustrated by the same broken line in the figure. The experimental points approach PFFM with increasing $\rho_{e0}U_0$, and move on toward EFM with reducing $\rho_{e0}U_0$. In the large mass flow rate operation, the appearance of non-accelerated droplets in the exhaust plume suggests that the flow structure is close to that of PFFM. The good agreement between experimental results and computational ones then indicates that PFFM properly describes the true flow structure of the spray thruster in the large mass flow rate operation. The tendency that the measured flow rate density approaches that of EFM in the small mass flow rate range implies that the transition from partially frozen state to equilibrium state occurs due to a decrease in the droplet diameter.

The following relation is known for ideal gas nozzle flow:

$$\dot{m}/A_t=\{2/(\gamma+1)\}^{1/(\gamma-1)}\{2\gamma/(\gamma+1)\}\rho_{e0}U_0. \tag{4–1}$$

The $\dot{m}/A_t$ is shown to be proportional to $\rho_{e0}U_0$ in this case. As for $\dot{m}/A_t$ in both EFM and PFFM, the least square regression analysis gives the following relation in the range of $\rho_{e0}U_0<100$ g/(scm^2):

$$\text{EFM}: \quad \dot{m}/A_t\propto(\rho_{e0}U_0)^{0.77}, \tag{4–2}$$

$$\text{PFFM}: \quad \dot{m}/A_t\propto(\rho_{e0}U_0)^{0.90}. \tag{4–3}$$

The $\rho_{e0}U_0$ dependency of $\dot{m}/A_t$ in both EFM and PFFM is small in comparison with that of ideal gas nozzle flow. This is explained by the following consideration. The strong evaporation taking place near the throat section results in an increase in the vapor mass flow rate. The flow with additional vapor mass causes choking at the throat with lower mass flow rate than that of the flow without evaporation. Furthermore, the additional vapor mass is increased with the total mass flow rate. As a result, the exponents of $\rho_{e0}U_0$ in Eq. (2-10), Eq. (4-2), and Eq. (4-3) become smaller than unity (1.0).

Figure 4-2 shows the relation between the thrust density and the reference thrust density described with evaporation chamber state variables. Both EFM and PFFM show the similar tendency. The experimental points are close to the simulation curve of PFFM. In the large mass flow rate range, the good agreement with the experimental results and simulation results of PFFM confirms that the flow structure in this range is well described by PFFM. In the small mass flow rate range, however, the following question may be forwarded: Why is the measured thrust close to that of PFFM in spite of the fact that the measured mass flow rate approaches that of EFM? This is explained as follows: Decreasing the mass flow rate results in a decrease in the droplet diameter, which supports the acceleration of liquid phase. Therefore the mean exhaust velocity is increased. Thrust is given by

$$F=\rho_{ex}U_{ex}^2A_e+P_{ex}A_e, \tag{4–4}$$

where ρ_{ex} and U_{ex} denote the mixture flow density and the mean flow velocity at the nozzle exit. P_{ex} is the static pressure. An approach to the flow structure of EFM decreases the mass flow rate $\rho_{ex}U_{ex}A_e$. But the mean flow velocity is increased.

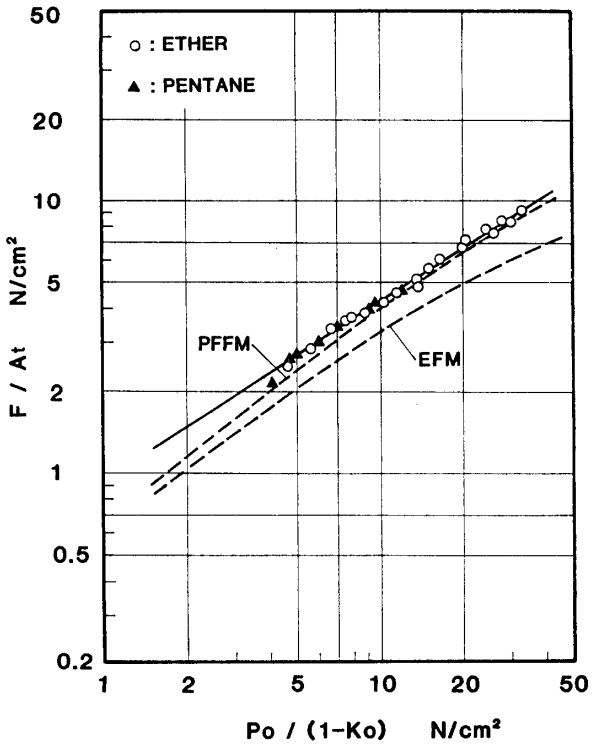

Fig. 4-2. Comparison of experimental results with numerical ones: characteristics of thrust density.

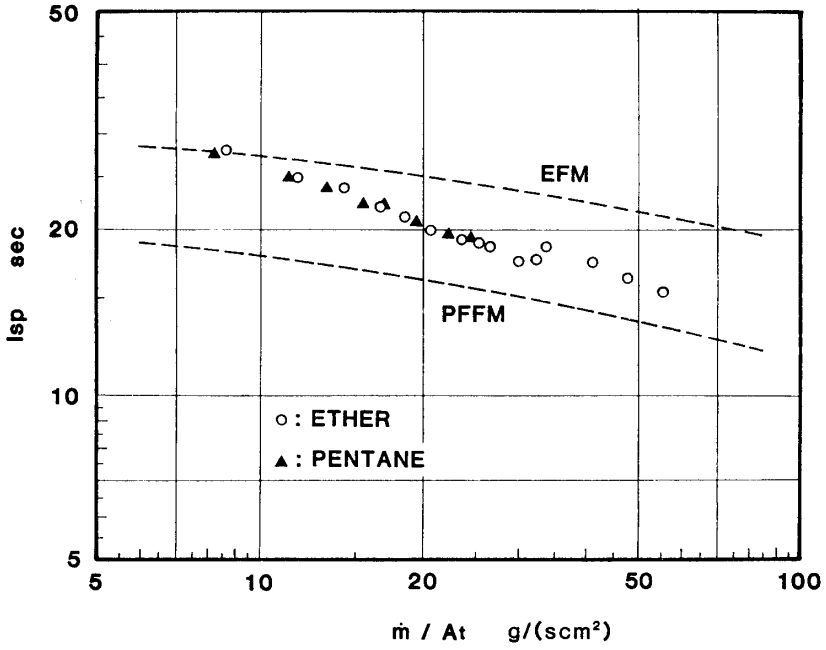

Fig. 4-3. Comparison of experimental results with numerical ones: characteristics of specific impulse.

Consequently, if an increase in the flow velocity compensates the decrease in the mass flow rate, the thrust is not decreased. The increase in the mean flow velocity is clearly shown in Fig. 4–3, in which the measured I_{SP} is almost equal to that of EFM when the mass flow rate density is lower than about 10 g/(scm^2).

The momentum thrust of ideal gas flow produced in a convergent nozzle is expressed by

$$F/A_t=\{2/(\gamma+1)\}^{1/(\gamma-1)}\{2\gamma/(\gamma+1)\}\rho_{e0}U_0^2. \tag{4–5}$$

Thrust is proportional to $\rho_{e0}U_0^2$. The $\rho_{e0}U_0^2$ dependency of thrust density in EFM and PFFM are given as follows:

$$\text{EFM}: \quad F/A_t\propto(\rho_{e0}U_0^2)^{0.62}, \tag{4–6}$$

$$\text{PFFM}: \quad F/A_t\propto(\rho_{e0}U_0^2)^{0.67}. \tag{4–7}$$

The exponents of $\rho_{e0}U_0^2$ in both models are smaller than unity. This trend is qualitatively explained by the following consideration. The thrust is expressed as a product of the mass flow rate and the mean exhaust velocity. As for the mass flow rate, the exponent of $\rho_{e0}U_0$ is smaller than unity as was shown in Eq. (4-2) and Eq. (4-3). The U_0 dependency of the mean exhaust velocity is explained as follows: Since an increase in U_0 corresponds to the increase in the mass flow rate, that is, the rise of liquid mass fraction, increasing U_0 reduces the mean exhaust velocity in both

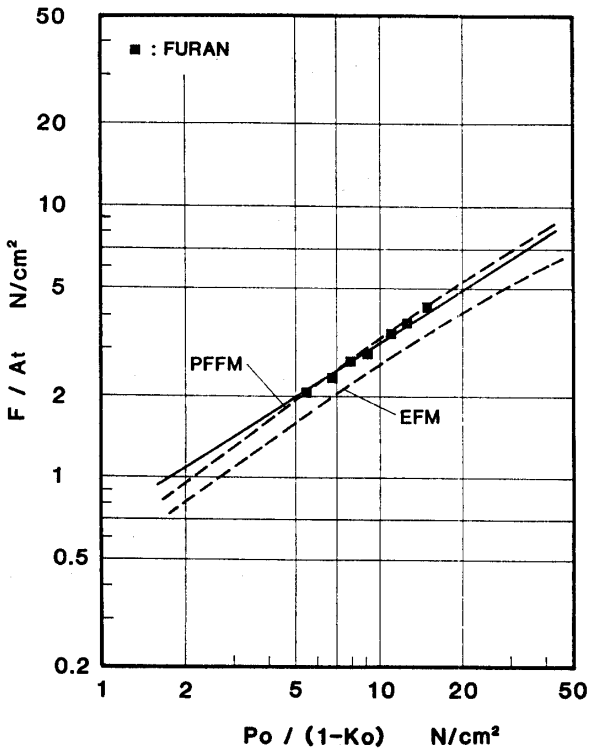

Fig. 4–4. Comparison of experimental results with numerical ones: characteristics of thrust density for Furan.

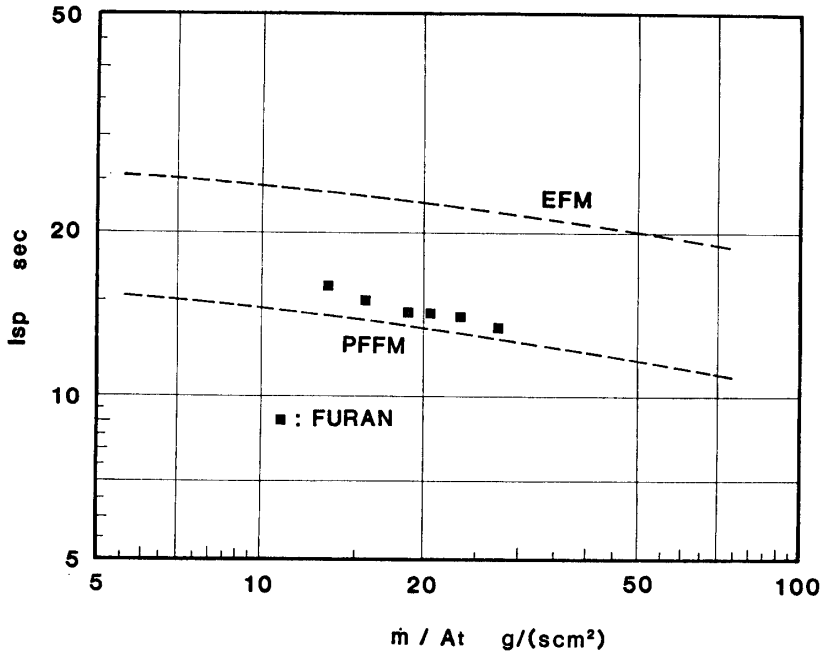

Fig. 4–5. Comparison of experimental results with numerical ones: characteristics of specific impulse for Furan.

EFM and PFFM for a given tank temperature operation. Hence the mean exhaust velocity has negative dependency on U_0. From these reasons, $\rho_{e0}U_0^2$ dependencies of thrust density in both EFM and PFFM are small in comparison with that of ideal gas nozzle flow.

Figures 4-4 and 4-5 show the thrust performance characteristics of Furan. The measured points are close to the calculated results in PFFM throughout the exprimental range. Even if the mass flow rate is decreasing, the transition from the partially frozen state to the equilibrium state is not observed clearly in this case. This is considered to be due to the large mass fraction of the liquid phase in the present operation.

4–2. Parametric Effects on Thrust Performance

The applicability of EFM and PFFM has been evaluated in the previous section by comparing the computational results with the experimental ones. It has been shown that EFM is suitable for the description of the flow structure in the small mass flow rate range, and that PFFM properly represents the flow structure in the large mass flow rate range. In the present section, various parametric dependencies of thrust performance are discussed by employing both EFM and PFFM.

4–2–1. Effect of chemical properties of propellant

Let us consider similar conditions of nozzle flow in the spray thruster. One condition is obtained by putting the liquid mass fraction in the evaporation chamber to be constant, thus let,

$$C_p(T_t - T_0)/Q_t(T_0) = \text{const.} \tag{4–8}$$

The other conditions are given from setting non-dimensional chemical properties of propellant to be unchanged:

$$C_p/R = \text{const.}, \tag{4–9}$$

$$Q_l(T)/RT_0: \quad \text{A function of } T. \tag{4–10}$$

Since $Q_l(T)$ is a weak function of temperature in the present experimental range, it is reasonably assumed that $Q_l(T)$ is represented by $Q_l(T_0)$. Consequently, the above three conditions are equivalent to the following ones.

$$T_0/T_t = \text{const.}, \tag{4–11}$$

$$C_p/R = \text{const.}, \tag{4–12}$$

$$Q_l(T_0)/(RT_0) = \text{const.} \tag{4–13}$$

Chemical properties of liquid are represented by only two parameters C_p/R and $Q_l(T_0)/(RT_0)$. Figure 4–6 shows C_p/R and $Q_l(T_0)/(RT_0)$ of various liquids, where T_t and T_0 are specified to be 293K and 273K, respectively. The solid line denotes non-dimensional exhaust velocity U^* as is marked with its value. When the molecular weights are identical, the higher quantity of C_p and lower quantity of $Q_l(T_0)$ lead to higher non-dimensional exhaust velocity. Then the higher the non-dimensional exhaust velocity is, the more effectively thrust is produced. In Fig. 4-6, all of the liquids are divided into three groups. Propane, Butane, Pentane, and Ethyl Ether belong to the first group, in which C_p/R is large, $Q_l(T_0)/(RT_0)$ is small, and non-dimensional exhaust velocity is high. The liquid in the first group is suitable for the propellant of spray thruster. Furan, Freon 11 and Ammonia belong to the second group, in which non-dimensional exhaust velocity is in the middle range. The third group is composed of Hydrazine, Methanole and Water. These liq-

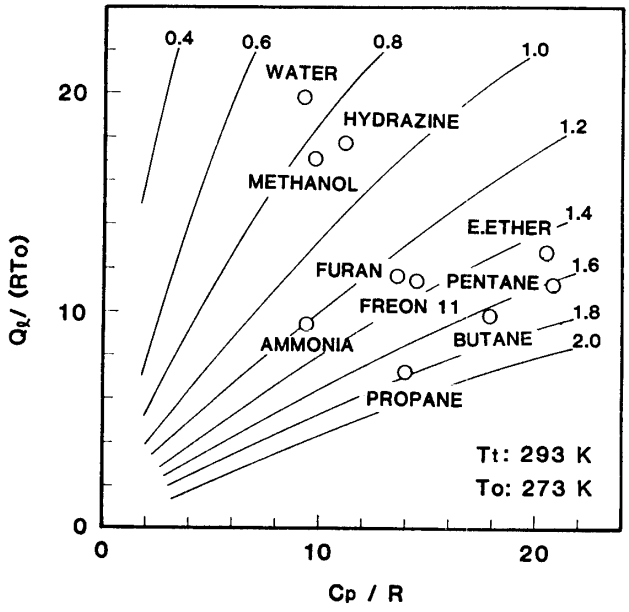

Fig. 4–6. Similar conditions in liquid properties.

uids have large latent heat of evaporation and then are not suitable for the propellant.

Next let us consider about the maximum propulsive energy converted from enthalpy of the liquid through the expansion into vacuum. In the spray thruster system, the following relation should exist for the steady operation:

$$T_f < T_e < T_0 < T_t < T_c, \tag{4-14}$$

where T_f is the freezing point of the liquid, T_e is the temperature at the nozzle exit, and T_c is the critical point. The lowest operational temperature is determined by a condition that the saturation vapor pressure goes down so low near the freezing point, and it is necessary to prevent the liquid from freezing on the nozzle wall. The maximum propulsive energy is obtained at the maximum flow velocity under the fixed mass flow rate condition. The maximum flow velocity is given by rewriting Eq. (3-17) with dimensional variables as follows:

$$U_{\max} = \left\{ 2T_f \int_{T_t}^{T_f} 1/T^2 \left(\int_{T_t}^{T} C_p dT \right) dT \right\}^{1/2}. \tag{4-15}$$

The maximum I_{SP} is defined by

$$I_{SP\max} = U_{\max}/g. \tag{4-16}$$

Figure 4-7 shows the maximum I_{SP} of various liquid propellants. Propane has the highest I_{SP} that is close to the maximum theoretical I_{SP} of Nitrogen which is represented by the broken line. Butane, Pentane, Ethyl Ether, and Ammonia follow to Propane in that order. Furan, because of its low heat capacity, and water, because of its high freezing point and large latent heat of evaporation, show low I_{SP}. It should be noted, however, that Propane, Butane, and Ammonia exist in gas phase

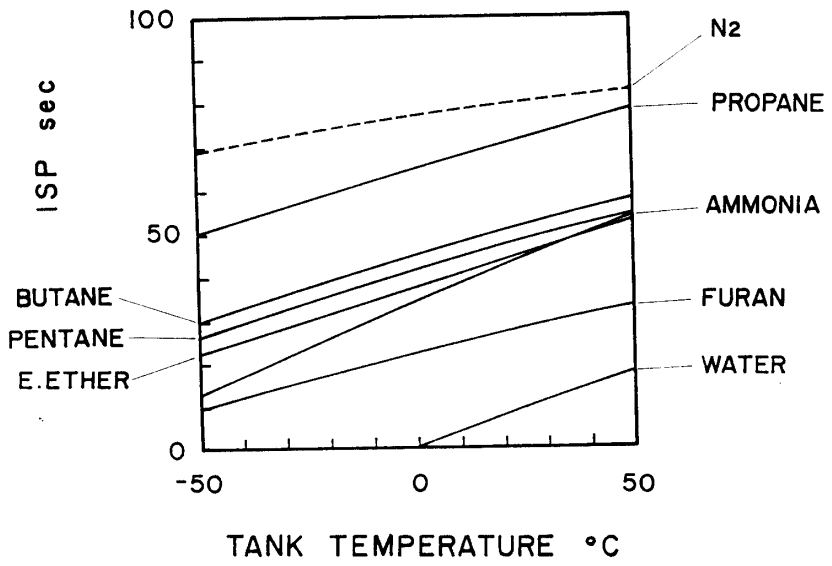

Fig. 4-7. Maximum theoretical I_{SP}.

under a standard state, which increases the difficulty in handling in comparison to the others.

4–2–2. Effect of nozzle dimension

Let us consider the effect of throat area on the thrust performance. It is assumed that the nozzle dimension is changed while maintaining similar configuration. If the mass flow rate is increased in proportion to the throat cross sectional area, an increase in the throat area does not cause any change in the state of the evaporation chamber and nozzle. However, if the throat area is changed under a fixed mass flow rate condition, the change in the mass flow rate density $\dot{m}/A_t$ is described as

$$\dot{m}/A_{t_1} \longrightarrow \dot{m}/A_{t_2}, \tag{4–17}$$

where subscript 1 denotes the initial nozzle dimension, and subscript 2 represents the altered nozzle dimension. Let $F(\dot{m})$ express the thrust produced at the mass flow rate of $\dot{m}$ and the throat cross sectional area of A_{t_1} for a given areal expansion ratio. The change in thrust corresponding to the change (4-17) is given by

$$F(\dot{m}) \longrightarrow F(\dot{m}A_{t_1}/A_{t_2})\cdot(A_{t_2}/A_{t_1}). \tag{4–18}$$

Then the change in I_{SP} is expressed as follows:

$$I_{SP_1} \longrightarrow I_{SP_2}, \tag{4–19}$$

where

$$I_{SP_1}=F(\dot{m})/(\dot{m}g), \tag{4–20}$$

$$I_{SP_2}=A_{t_2}F(\dot{m}A_{t_1}/A_{t_2})/(\dot{m}A_{t_1}g). \tag{4–21}$$

The I_{SP_2}/I_{SP_1} is plotted against A_{t_2}/A_{t_1} for Ethyl Ether in Fig. 4-8. The calculation condition is that the tank temperature is 293 K, mass flow rate is 20 g/sec, and A_{t_1} is

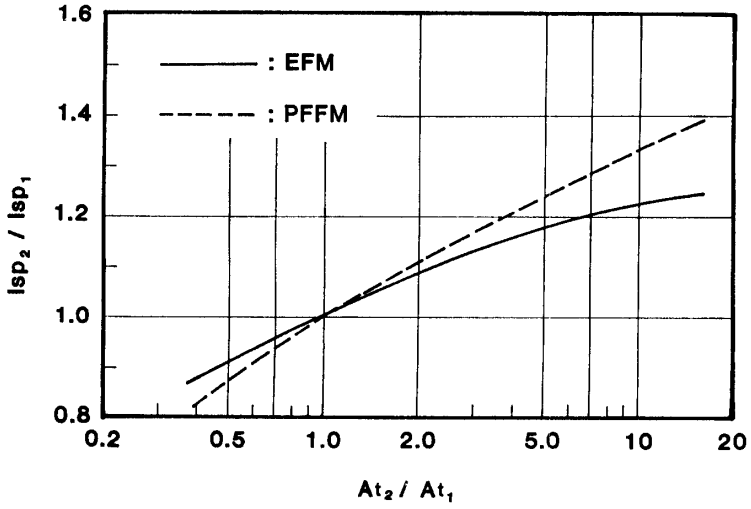

Fig. 4-8. Effect of nozzle dimension on the I_{SP}.

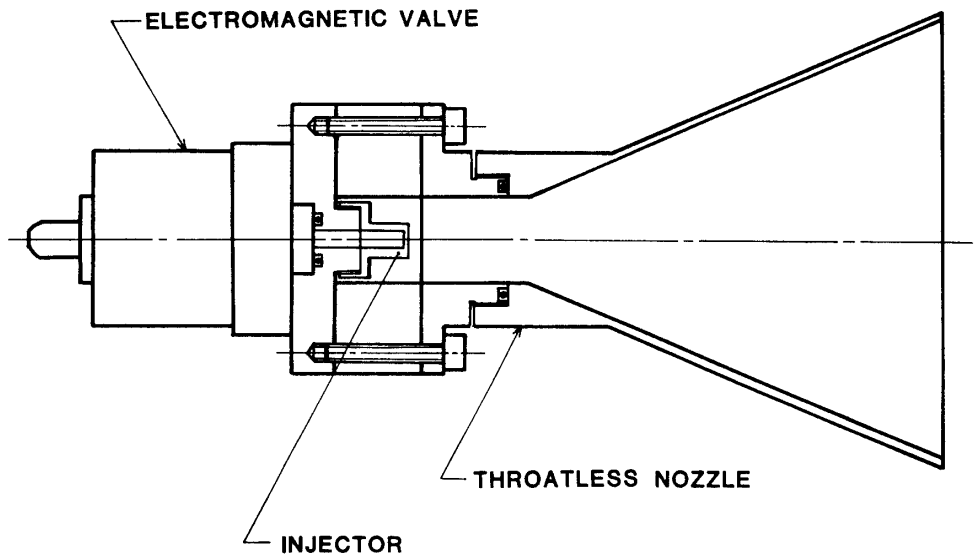

Fig. 4-9. Schematic configuration of throatless nozzle.

0.7854 cm^2. The propellant is Ethyl Ether. The solid line and the broken line denote EFM and PFFM, respectively. It is shown that large cross sectional area is preferable in order to increase the thrust performance in both EFM and PFFM. It is because an increase in the throat radius corresponds to a decrease in the liquid mass fraction in the evaporation chamber for a given mass flow rate. Increasing the throat radius is also preferable from the view point of vapor-liquid relaxation phenomena, since the nozzle flow structure approaches that of EFM owing to the increase in the stay time of droplets in the nozzle.

The radius of the evaporation chamber can not be infiinitely increased, so that the maximum obtainable throat radius is limited to the radius of the evaporation chamber. Therefore the above investigation suggests that a throatless nozzle as shown in Fig. 4-9 is most suitable for the spray thruster.

4–2–3. Effect of operational temperature

Spray thruster is operated in the temperature range from the freezing point to the critical point of the liquid propellant in principle. However, the saturation pressure is too high at the temperature close to the critical point. The liquid easily freezes under the freezing point. Therefore the middle temperature range is suitable for the operation of the spray thruster. Particularly, the room temperature range is preferable from the view point of handling.

Figure 4–10 shows the thrust performance of spray thruster using Ethyl Ether in the room temperature range. The thrust and I_{SP} are calculated from EFM. The expansion ratio of nozzle is specified to be 100. The I_{SP} is gradually increased with decreasing the evaporation chamber temperature due to a decrease in the liquid mass fraction as was mentioned previously. Likewise the I_{SP} is increased with the tank temperature. About 5 sec gain in I_{SP} is obtained by 20°C increase in the tank temperature. On the other hand, the thrust is rapidly decreased with T_0. An increase

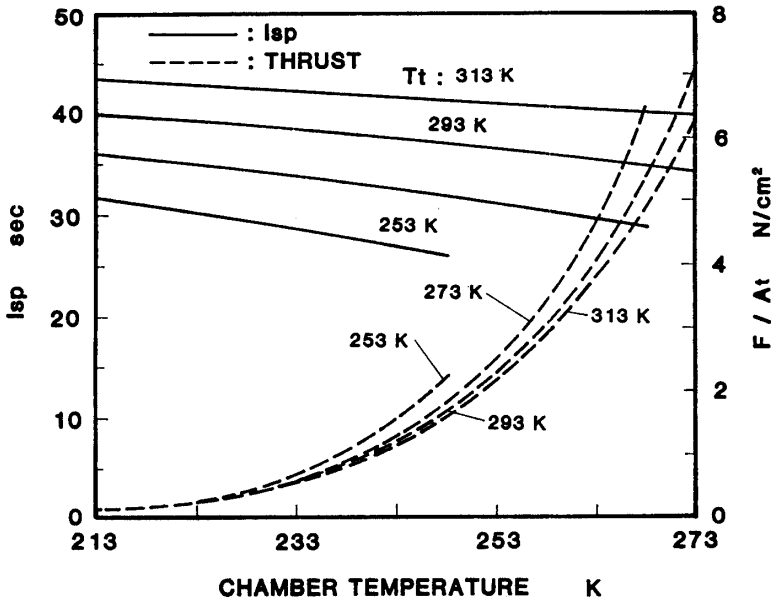

Fig. 4–10. Effect of operational temperature on the thrust performance.

in T_t results in a slight increase in the thrust for a given T_0. From these results, the spray thruster is characterized as its large thrust magnitude and variable thrust capability. These characteristics are not seen in subliming solid rocket and vaporizing liquid rocket systems.

It is obvious that we could improve the thrust performance of the spray thruster by utilizing an external heat source like resistojets. There are two kinds of heating, that is, isobaric heating and isochoric heating. In the isobaric heating, the liquid changes from state A to state C in Fig. 1-1. In the isochoric heating, the liquid changes from state A to the critical point along the saturation liquid line. If the input power is the same, both heating methods result in the same thrust performance.

By using EFM, let us estimate thrust efficiency of spray thruster with external heat source. The liquid is assumed to be stored initially at temperature T_{t_0} When the liquid is heated to its temperature of T_t, the following thrust efficiency can be defined:

$$\eta_{ST}=\{F^2/(2\dot{m})-F_0^2/(2\dot{m})\}/\{\dot{m}C_p(T_t-T_{t_0})\}, \tag{4–22}$$

Table 4–1. Heating efficiency of spray thruster.

T_t (K)	Thrust (N)	$F^2/(2\dot{m})$ (J/s)	Input Power (J/s)	η_{ST}
288	0.797	158.9	0.0	—
318	0.873	190.0	93.7	0.34
338	0.944	223.0	187.5	0.34
358	1.011	255.7	281.3	0.34
378	1.074	288.7	375.0	0.35

$\dot{m}=2$ g/sec

where F_0 is the thrust at the tank temperature of T_{t_0}. The denominator denotes the input energy, and the numerator indicates an increase in the propulsive energy. The thrust efficiency is listed in Table 4-1, in which Ethyl Ether is used as the propellant, the expansion ratio is 100, the throat diameter is 1 cm, and T_{t_0} is specified to be 298 K. It is shown that η_{ST} is almost constant at 0.34, regardless of the magnitude of the input energy.

4–2–4. Effect of mass of the propellant storage system

For the accurate evaluation of a thruster system, not only the thrust performance but also the system mass are employed as the criteria. Effective specific impulse is then introduced as the combined criterion of thrust performance and system weight.

The total rocket system weight is divided into the following components:

W_0: Total mass of a rocket system
W_{PL}: Payload mass
W_P: propellant mass of an auxiliary thruster system
W_S: structural mass of an auxiliary thruster system

The mass ratio is defined as

$$\alpha = W_{PL}/W_0, \tag{4–23}$$

$$\beta = 1/(1+W_P/W_S). \tag{4–24}$$

α is called payload ratio. The characteristic velocity of the auxiliary thruster system is given by

$$\Delta V = -gI_{SP}\ln\{1-(1-\alpha)(1-\beta)\}, \tag{4–25}$$

where I_{SP} is the specific impulse of the auxiliary thruster. Generally speaking, the mass of the auxiliary thruster system is smaller than the mass of the total system so that the following relation is applicable:

$$1-\alpha \ll 1. \tag{4–26}$$

Eq. (4-25) is rewritten using the above relation as

$$I_{SP} = \Delta V(1+W_P/W_S)/\{g(1-\alpha)\}. \tag{4–27}$$

The effective specific impulse is then defined by

$$I_e = I_{SP}/(1+W_S/W_P) = \Delta V/\{g(1-\alpha)\}. \tag{4–28}$$

The above equation shows that the payload ratio is increased with the effective specific impulse I_e. Therefore, the higher I_e is, the better is the system.

Next, it is assumed that the propellant storage tank is spherical and is designed not to be broken by the inner pressure. The mass of the tank W_t is obtained for a gas propellant as follows:

$$W_t/W_p = 3\rho_w RT_t/(2S_w). \tag{4–29}$$

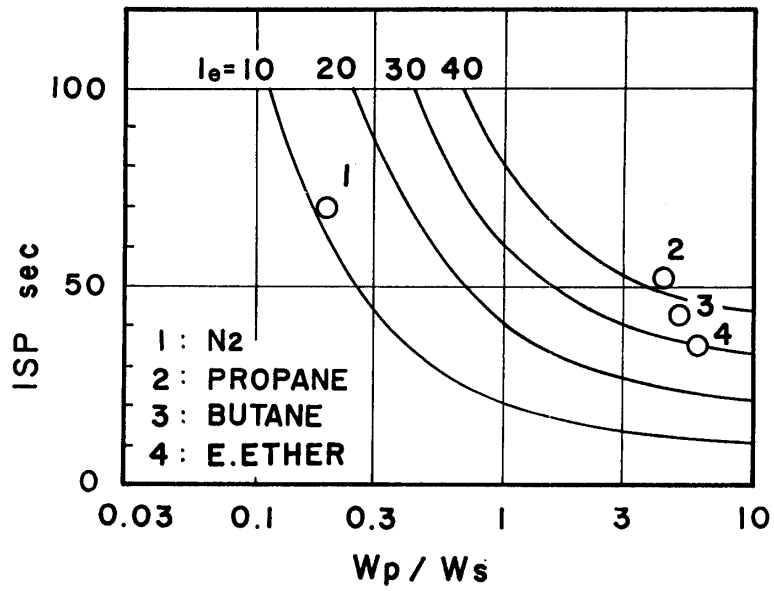

Fig. 4–11. Effective specific impulse.

In a case of liquid propellant, it is given by

$$W_t/W_p=3\rho_w P_t/(2S_w\rho_L). \tag{4–30}$$

where S_w and ρ_w are allowable tensile strength and density of the tank material, respectively. R is the gas constant, ρ_L is the liquid density, and P_t is the pressure in the storage tank.

Figure 4–11 shows I_e of spray thruster and Nitrogen cold gas jet which is widely used as an attitude control motor. The calculation condition is that ρ_w is 7.9 g/cm^3, Sw is 196 N/mm^2, P_t is 1.96 MPa, T_t is 300 K, and the areal expansion ratio is specified to be 100. The structural mass W_s is assumed to be equal to W_t. It is shown that the spray thrusters have higher values of I_e than that of a Nitrogen cold gas jet. This is due to the large liquid densities of Propane, Butane, and Ethyl Ether. In the spray thruster systems, Propane's system is the most excellent for the I_e performance.

5. Conclusion

The evaporation process of liquid exposed to a vacuum environment has been studied for propulsion application. A new thruster system called "Spray Thruster" has been presented. The spray thruster positively utilizes the evaporation process of liquid propellant to produce a gaseous working fluid. The thrust performance has been investigated both experimentally and theoretically.

The experimental models of spray thruster were tested in the wide range of the mass flow rate. Ethyl Ether, Pentane, and Furan were used as the propellants. It has been shown that spray thruster is operated well in a vacuum environment without any energy additions. The thrust performance characteristics are described as

follows: The discharge coefficient C_D is on the order of 0.1 sec^{-1} and is increased with the mass flow rate due to the increase in the liquid mass fraction. The thrust coefficient C_F is almost constant to be 2.5. The specific impulse I_{SP} is increased with decreasing the mass flow rate. It reaches 28 sec at mass flow rate of 6.9 g/sec for Ethyl Ether. The dependency of C_D, C_F and I_{SP} on the evaporation chamber condition is obtained as follows:

(1) $C_D \propto [1/\{(1-K_0)\sqrt{RT_0}\}]^{0.94}(1/P_0)^{0.06}$,

(2) $C_F \propto [1/(1-K_0)]^{0.65}(1/P_0)^{0.35}$,

(3) $I_{SP} \propto \{(1-K_0)/P_0\}^{0.29}(RT_0)^{0.47}$.

In the large mass flow rate operation, non-accelerated droplets were observed to disperse at the nozzle wall edge. It suggests that a thin liquid layer is formed over the nozzle inner wall and that the thrust loss is partly attributed to this layer.

On the basis of the experimental results, two kinds of flow models have been introduced to examine the more detailed mechanism of thrust production. They are Equilibrium Flow Model (EFM) and Partially Frozen Flow Model (PFFM). The PFFM is the newly developed concept in which the pressure is in a saturation equilibrium condition, the droplet temperature is equal to the vapor temperature, and the droplet velocity is frozen. Comparison of the experimental results with theoretical ones has shown that EFM simulates the flow structure properly in the low mass flow rate range and that PFFM represents the flow structure in the large mass flow rate operation. The transition from PFFM to EFM is mainly due to the decrease in the droplet diameter associated with the decrease in the liquid mass fraction. The droplet frozen velocity is estimated to be about 20 m/sec. The allowable droplet diameter is evaluated by considering the breakup of droplets in the nozzle. The maximum value lies in the droplet diameter range of PFFM.

Parametric effects on the thrust performance have been studied by using EFM and PFFM. It has been shown that the nozzle flow field is characterized by two nondimensional parameters, C_p/R and $Q_l(T_0)/(RT_0)$. The large quantity of C_p/R and the small quantity of $Q_l(T_0)/(RT_0)$ are suitable features for the propellant. The preferable liquids are Propane, Butane, Pentane and Ethyl Ether, the maximum theoretical *Isp* of which are 72, 52, 49 and 45 seconds at the propellant temperature 300 K, respectively. It has been also shown that the nozzle dimension influences the thrust performance for a given mass flow rate condition. The large throat diameter is desirable, so that the throatless nozzle configuration is proposed. According to a practical point of view, the spray thruster system has been shown to be superior to Nitrogen cold gas jet system owing to the large propellant density.

Appendix 1. Time Constants of Relaxation Phenomena

(A) τ_s: Time constant of mass transfer

The evaporating mass flow rate per unit area is generally expressed by

$$\dot{m}_{ev}=\frac{P}{\sqrt{2\pi RT}}\left\{C_1\frac{P_s(T_p)-P}{P}+C_2\frac{T-T_p}{T}\right\}, \tag{A1-1}$$

C_1 and C_2 are the accomodation constants. In continuum, C_2 is generally specified to be zero [22]. It is assumed that the liquid phase is composed of small spherical droplets with the radius of r_p. The evaporating mass flow rate is then given by

$$\Phi/\rho_p=4\pi r_p^2\dot{m}_{ev}/(4\pi r_p^3 M_p/3), \tag{A1-2}$$

where ρ_p is the density of the liquid phase, M_p is the material density of the liquid, and ρ is the density of the gas phase. The substitution of Eq. (A1-1) into Eq. (A1-2) results in

$$\Phi/\rho_p=(3\rho a\alpha/M_p r_p)\cdot(P_s-P)/P, \tag{A1-3}$$

where

$$\alpha=C_1/\sqrt{2\pi\gamma}, \tag{A1-4}$$

$$a=\sqrt{\gamma RT}. \tag{A1-5}$$

The time constant of mass transfer is then expressed by

$$\tau_s=M_p r_p/(3\rho a\alpha). \tag{A1-6}$$

In the case of free molecular flow which corresponds to $C_1=1$, α is calculated to be 0.33 for $\gamma=1.4$.

(B) τ_m: Time constant of momentum transfer

In the gas-particle flows, the particle phase is accelerated by the viscous drag force. The magnitude of the force is expresed by

$$F=(1/2)C_{Dp}n_p\rho(U-U_p)|U-U_p|\pi r_p^2, \tag{A1-7}$$

where C_{Dp} is the proportional constant, n_p is the number density of particle, U and U_p are the velocity of gas and particle phases, respectively. When the particle is so small that the Stokes drag law is applicable, the C_{Dp} is given by

$$C_{Dp}=24/\mathrm{Re}, \tag{A1-8}$$

where

$$\mathrm{Re}=2r_p\rho|U-U_p|/\mu. \tag{A1-9}$$

Substituting Eqs. (A1-8) and (A1-9) into Eq. (A1-7), we have

$$F=9\mu/(2M_p r_p^2)\cdot\rho_p(U-U_p). \tag{A1-10}$$

The time constant of momentum transfer is then obtained as follows:

$$\tau_m=2M_p r_p^2/(9\mu). \tag{A1-11}$$

The τ_m is proportional to the square of the particle radius.

(C) τ_h: Time constant of heat transfer by convection

The heat transfer between the gas and particle phases per unit volume and unit time is expressed by

$$Q_p = n_p \cdot \lambda \cdot 4\pi r_p^2 (T - T_p), \tag{A1-12}$$

where λ is the proportional constant, which is described by

$$\lambda = \kappa_g N_u / (2r_p). \tag{A1-13}$$

The κ_g is the coefficient of heat transfer by conduction in the gas phase, and N_u is the Nuselt number which is specified to be 2.0 when the Reynolds number is enough small. The time constant of heat transfer by convection is, hence, given by

$$\tau_h = M_p r_p^2 C_p / (3\kappa_g), \tag{A1-14}$$

where C_p is the heat capacity of the particle phase. The ratio of τ_h and τ_m is described by

$$\tau_h / \tau_m = (3/2) P_r (C_p / C_{pg}), \tag{A1-15}$$

where P_r is the Prandtle number, and C_{pg} is the heat capacity of the gas phase. Both P_r and C_p/C_{pg} lie in the order of unity, so that τ_h and τ_m are on the same order of magnitude.

(D) τ_c: Time constant of heat transfer by conduction

Since the evaporating mass flow rate strongly depends on the surface temperature of the liquid, the temperature distribution within a droplet is an important factor to be considered. The time constant of heat transfer by conduction is approximately given by

$$\tau_c = M_p C_p r_p^2 / (\pi^2 \kappa_p), \tag{A1-16}$$

where κ_p is the coefficient of heat transfer by conduction within a droplet.

Appendix 2. Fundamental Equations of Gas-Particle Flows

(A) Fundamental Equations

The conservation equations governing the steady quasi-one dimensional flow of the gas-particle mixture are derived under the following assumptions:

(1) The total mass and the total energy of the system remain constant.
(2) The gas is perfect gas and inviscid except for its interaction with the particles.
(3) The thermal motion of the particles is negligible.
(4) The volume occupied by the particles is negligible.
(5) The particle do not interact each other.
(6) The characteristics of an actual shape and size distribution of particles can be represented by spherical particles of a single size.

(7) The only force on the particles is viscous drag force which is subject to Stokes drag law.

The fundamental equations are given as follows:

mass conservation:

$$d(\rho UA)/dX=A\Phi, \tag{A2-1}$$

$$d(\rho_p U_p A)/dX=-A\Phi, \tag{A2-2}$$

momentum conservation:

$$\rho UdU/dX+\rho_p U_p dU_p/dX+dP/dX-\Phi(U_p-U)=0, \tag{A2-3}$$

$$\rho_p U_p dU_p/dX=\rho_p/\tau_m\cdot(U-U_p), \tag{A2-4}$$

energy conservation:

$$\rho UA(h_g+U^2/2)+\rho_p U_p A(h_p+U_p^2/2)=E_0, \tag{A2-5}$$

$$\rho_p U_p dh_p/dX=\rho_p/\tau_h\cdot(T-T_p)-\Phi Q_l, \tag{A2-6}$$

equation of state:

$$P=\rho RT, \tag{A2-7}$$

where τ_m and τ_h are the time constants of momentum and heat transfers between the gas and particle phases. Φ is the evaporating mass flow rate per unit volume. h_g and h_p is the enthalpy of the gas and particle phases, respectively. When the mixture is composed of vapor and its condensed phase, the following relation is obtained:

$$h_g(T)=h_p(T)+Q_l(T), \tag{A2-8}$$

where Q_l is the latent heat of evaporation. In the present analysis, it is assumed that the heat capacity of the liquid C_p remains constant, and the heat capacity of the vapor C_{pg} is expressed by

$$C_{pg}=C_p+dQ_l/dT. \tag{A2-9}$$

The specific heat ratio is, hence, given by

$$\gamma=C_{pg}/(C_{pg}-R). \tag{A2-10}$$

Since dQ_l/dT is always negative, the heat capacity of vapor is smaller than the heat capacity of liquid in general.

(B) Derivation of Eqs. (3–46) and (3–47)

Differentiation of Eq. (3-47) results in

$$d\rho^*/\rho^*+dU^*/U^*+dA^*/A^*-A^*\Phi^*dX^*/(\rho^*U^*A^*)=0. \tag{A2-11}$$

From the differential form of Eq. (3-44) and Eq. (3-14), the density term in the above equation is rewritten by

$$d\rho^*/\rho^* = (Q_l^*/T^* - 1)dT^*/T^*. \tag{A2-12}$$

From the relations: $A^*\Phi^*dX^* = -\dot{m}^*dK$ and $\rho^*U^*A^* = (1-K)\dot{m}^*$, the third term in Eq. (A2-11) becomes

$$A^*\Phi^*dX^*/(\rho^*U^*A^*) = -dK/(1-K). \tag{A2-13}$$

Substituting Eqs. (A2-12) and (A2-13) into Eq. (A2-11), we have

$$dU^*/U^* + dA^*/A^* + (Q_l^*/T^* - 1)dT^*/T^* + dK/(1-K) = 0. \tag{A2-14}$$

The momentum conservation equation is given by

$$\frac{dU^*}{U^*} = -\frac{(1-K_0)}{\rho^*U^{*2}}dP^* + \frac{U_p^* - U^*}{\rho^*U^{*2}}\cdot\Phi^*dX^*. \tag{A2-15}$$

From Eqs. (3-14) and (A2-13), the above equation is rewritten as follows:

$$\frac{dU^*}{U^*} = -\frac{Q_l^*}{U^{*2}}\cdot\frac{dT^*}{T^*} + \frac{U^* - U_p^*}{U^*}\cdot\frac{dK}{1-K}. \tag{A2-16}$$

Differentiating Eq. (3-43), we have

$$\left(\frac{U^{*2}}{2} - \frac{U_p^{*2}}{2} + Q_l^*\right)\frac{dK}{1-K} = \frac{C_p^*}{1-K}dT^* + \frac{dQ_l^*}{dT^*}dT^* + U^*dU^*. \tag{A2-17}$$

Elimination of dK from both Eqs. (A2-16) and (A2-17) results in

$$\left(\frac{Q_l^*}{U^{*2}} - \frac{\theta_1}{\theta_2}\frac{C_p^*T^*}{1-K} - \frac{\theta_1}{\theta_2}T^*\frac{dQ_l^*}{dT^*}\right)\frac{dT^*}{T^*} = -\left(1 - \frac{\theta_1}{\theta_2}U^{*2}\right)\frac{dU^*}{U^*}, \tag{A2-18}$$

where

$$\theta_1 = (U^* - U_p^*)/U^*, \tag{A2-19}$$

$$\theta_2 = U^{*2}/2 - U_p^{*2}/2 + Q_l^*. \tag{A2-20}$$

Substituting Eqs. (A2-17) and (A2-18) into Eq. (A2-14), we finaly obtain Eqs. (3-46) and (3-47) as follows:

$$(1 - M_f^{\,2})dU^*/U^* + dA^*/A^* = 0, \tag{A2-21}$$

where

$$M_f^{\,2} = -\frac{1}{\theta_2}\left[U^{*2} + \left\{\theta_2\left(\frac{Q_l^*}{T^*} - 1\right) + \frac{C_p^*T^*}{1-K} + T^*\frac{dQ_l^*}{dT^*}\right\} \times \frac{1 - (\theta_1/\theta_2)U^{*2}}{(\theta_1/\theta_2)\{C_p^*T^*/(1-K) + T^*(dQ_l^*/dT^*)\}\cdot(Q_l^*/U^{*2})}\right]. \tag{A2-22}$$

REFERENCES

[1] Sutherland, G. S. and Maes, M. E., "A Review of Microrocket Technology: 10^{-6} to 1 lbf Thrust," Journal of Spacecraft and Rockets, Vol. 3, August 1966, pp. 1153–1165.

[2] Hardt, A. P., Foley, W. M. and Brandon, R. L., "The Chemistry of Subliming Solids for Micro Thrust Engines," AIAA Paper No. 65–595, June 1965.

[3] Day, B. P. and Hastings, R., "Some Cold Gas Auxiliary Jet Control Mechanisms and Propellants for Use in Earth Satellites," R.A.E. Technical Note GW580, 1961.

[4] Tinling, B. E., "Measured Steady-State Performance of Water Vapor Jets for Use in Space Vehicle Attitude Control System," NASA TN D-1302, May 1962.

[5] Hill, P. G., "Condensation of Water Vapor during Supersonic Expansion in Nozzles," Journal of Fluid Mechanics, Vol. 25, 1966, pp. 593–620.

[6] Chmielewski, T. and Sherman, P. M., "Effect of a Carrier Gas on Homogeneous Condensation in a Supersonic Nozzle," AIAA Journal, Vol. 8, April 1970, pp. 789–793.

[7] Wegener, P. P., Clumpner, J. A. and Wu, B. J. C., "Homogeneous Nucleation and Growth of Ethanol Drops in Suppersonic Flow," The Physics of Fluids, Vol. 15, November 1972, pp. 1869–1876.

[8] Rudinger, G., "Fundamentals of Gas-Particle Flow," Handbook of Powder Technology, Vol. 2, 1980.

[9] Kliegel, J. R., "Gas-Particle Nozzle Flows," The 9th Symposium on Combustion, Academic Press, New York, 1963, pp. 811–826.

[10] Doi, T., "Gas-Particle Nozzle Flows and Optimum Nozzle Shape," ISAS Report No. 596, Tokyo Japan, November 1981.

[11] Chang, I. C., "One- and Two-Phase Nozzle Flows," AIAA Journal, Vol. 18, December 1980, pp. 1455–1461.

[12] Marble, F. E., "Some Gas Dynamic Problems in the Flow of Condensing Vapors," Astronautica Acta, Vol. 14, 1969, pp. 585–614.

[13] Glenn, L. A., "Stationary Radial Source Flow of Liquid Particles into Vacuum," AIAA Journal, Vol. 7, March 1969, pp. 443–450.

[14] Glenn, L. A., "Recondensation from a Particle-Vapor Source Flow into Vacuum," AIAA Journal, Vol. 7, April 1969, pp. 593–597.

[15] Mikatarian, R. R. and Anderson, R. G., "An Experimental Investigation of a Liquid Jet Expelled into a Vacuum," Journal of Spacecraft and Rockets, Vol. 3, February 1966, pp. 267-268.

[16] 長友信人, "姿勢制御エンジン試験装置について", 宇宙航空研究所報告, 第7巻, 第1号 (A) 1971年1月.

[17] Crocco, L. and Cheng, S. I., "Theory of Combustion Instability in Liquid Propellant Rocket Motors," Butterworths Scientific Publications, 1956, pp. 25–72.

[18] 日本航空宇宙学会, "航空宇宙工学便覧", 丸善株式会社.

[19] Spisz, E. W., Brinich, P. F. and Jack, J. R., "Thrust Coefficients of Low-Thrust Nozzles," NASA TN D-3056, October 1965.

[20] Kunudsen, M., "The Kinetic Theory of Gases," Methuen, 1933.

[21] Ytrehus, T., "Theory and Experiments on Gas Kinetics in Evaporation," 10th International Symposium on Rarefied Gas Dynamics, July 1976, pp. 1197–1211.

[22] Shankar, P. N., "Kinetic Theory of Steady Condensation," Journal of Fluid Mechanics, Vol. 40, 1970, pp. 385–400.

[23] Lane, W. R., "Shatter of Drops in Streams of Air," Industrial and Engineering Chemistry, Vol. 43, No. 6, June 1951, pp. 1312–1324.

[24] Hanson, A. R., Domich, E. G. and Adams, H. S., "Shock Tube Investigation of the Break-up of Drops by Air Blasts," The Physics of Fluids, Vol. 6, No. 8, August 1963, 1070–1080.

[25] Gonor, A. L. and Zolotova, N. V., "Spreading and Break-up of a Drop in a Gas Stream," Acta Astronautica, Vol. 11, No. 2, 1984, pp. 137–142.

[26] Bartlett, R. W. and Delaney, L. J., "Effect of Liquid Surface Tension on Maximum Particle Size in Two-Phase Nozzle Flow," Pyrodynamics, Vol. 4, 1966, pp. 337–341.
[27] Clift, R., Grace, J. R. and Weber, M. E., "Bubbles, Drops, and Particles," Academic Press, 1978.
[28] Gordon, G. D., "Mechanism and Speed of Breakup of Drops," Journal of Applied Physics, Vol. 30, No. 11, November 1959, pp. 1759–1761.
[29] Morrell, G., "Breakup of Liquid Jets by Transverse Shocks," Eighth Symposium on Combustion, pp. 1059–1068.
[30] "Handbook of Chemistry and Physics," 61st Edition, CRC Press, 1980.
[31] 日本化学会, "化学便覧", 丸善株式会社.
[32] 化学工学協会, "化学工学便覧", 丸善株式会社.